Published in Lithos 106, issue 1-2, 93-109, 2008
which should be used for any reference to this work

Tectonic evolution of the Betic–Rif arc: New constraints from $^{40}Ar/^{39}Ar$ dating on white micas in the Temsamane units (External Rif, northern Morocco)

F. Negro [a,*], J. de Sigoyer [a], B. Goffé [a], O. Saddiqi [b], I.M. Villa [c,d]

[a] *Laboratoire de Géologie, UMR 8538 du CNRS, Ecole Normale Supérieure, 24 rue Lhomond, 75005 Paris, France*
[b] *Département de Géologie, Faculté des Sciences, Université Hassan II Aïn Chock BP 5366 - Maârif Casablanca, Morocco*
[c] *Institut für Geologie, Universität Bern, Baltzerstrasse 3, 3012 Bern, Switzerland*
[d] *Dipartimento di Scienze Geologiche e Geotecnologie, Università di Milano Bicocca, 20126 Milano, Italy*

Keywords:
Alboran
Betics
Rif
Ar–Ar
Temsamane
Morocco

A B S T R A C T

The Betic–Rif orogen, at the western end of the Mediterranean, is a key region to improve our knowledge on the Africa–Eurasia convergence. The Temsamane units, in spite of their external position in the Rif (northern Morocco), underwent medium-pressure low-temperature (MP–LT) conditions (ca. 7–9 kbar; 330–430 °C). We propose a new tectonic and metamorphic evolution scenario for the Rif (southern) branch of the orogen on the basis of first $^{40}Ar/^{39}Ar$ dating on petrologically and structurally characterized white micas. Three groups of $^{40}Ar/^{39}Ar$ ages are observed: (1) Chattian or older Si-rich (highest-pressure) mica relics, (2) 15–12.5 Ma corresponding to the micas defining the foliation and (3) Messinian or younger late micas and alteration. We propose that the MP–LT metamorphic event in the External Rif is Oligocene in age, highlighting a subduction event during this period which could be almost contemporaneous with the burial of HP–LT units from the internal Rif (Alboran Domain). The exhumation of these units characterized by an intense E–W stretching and by top-to-the-west shear senses, is Middle to Late Miocene in age. We propose a correlation of tectonic and metamorphic events at the Betic–Rif arc scale. We argue that the exhumation of the external units of the Rif (1) is younger than that of the Alboran Domain (internal) unit of the Rif, and mirrors a different tectonic setting, but (2) strongly resembles to that documented in the lower Alboran Domain units of the Betics. We show that a regional E–W extension is recorded on both sides of the Betic–Rif arc during the Middle Miocene. This extension probably reflects back-arc deformation of an eastward dipping subduction that retreated westward during the Middle to Late Miocene in the Western Mediterranean.

1. Introduction

The building of the Rif (northern Morocco) and the Betics (southern Spain), which represent the western termination of the Alpine orogenic system, has been the subject of many debates and several hypotheses are proposed to explain the formation of the Betic–Rif arc including: (1) convective removal of subcontinental lithosphere (Platt & Vissers, 1989; Platt et al., 2003a, Platt et al., 2006), (2) lithospheric delamination (Seber et al., 1996; Calvert et al., 2000; Tubía et al., 2004), (3) slab break off (Blanco and Spakman, 1993; Zeck, 1996) or (4) roll-back of an east dipping subduction zone (e.g. Lonergan and White, 1997; Frizon de Lamotte et al., 2000; Faccenna et al., 2004; Jolivet et al., 2006). The internal zones (Alboran Domain) (Fig. 1) of this orogen recorded high pressure–low temperature (HP–LT) (Gómez-Pugnaire and Fernandez Soler, 1987; Goffé et al., 1989) metamorphism generally considered to be Eocene–Oligocene in age (e.g. Platt et al., 2005; Michard et al., 2006), but more recently dated as Miocene in the lower Alboran Domain units (Platt et al., 2006). This event is overprinted during the early Miocene by HT–LP metamorph-ism related to the crustal extension that follow the shortening, and affected the whole Alboran Domain units (Balanyá et al., 1997; Platt et al., 2003a; Negro et al., 2006). This high thermal event reset most of isotopic systems in the whole area (e.g. Zeck et al., 1992; Platt et al., 2003a) and the betico–rifan accretionnary wedge early building stages remain difficult to constrain. Furthermore, even if several geochrono-logical studies have been carried out to constrain the Alboran Domain metamorphic evolution, data are lacking in the RExternalece nt Rif.studies show that the Temsamane units (External Rif), in spite of their external position in the Rif, underwent medium-pressure low-temperature (MP–LT) conditions (ca. 7–9 kbar; 330–430 °C). We propose that these metamorphic conditions are due to the subduction of Temsamane units as it is proposed for the high pressure units of the internal Rif (Negro et al., 2007). The exhumation of Temsamane units, which is characterized by an intense ~E–W stretching and by top-to-the-west shear senses, looks like the one documented in the core of the internal Betics (Galindo-Zaldívar et al., 1989; García-Dueñas et al., 1992; Jabaloy et al., 1993; Martínez-Martínez and Azañon, 1997; Martínez-

* Corresponding author. Present address: Institut de Géologie, Université de Neuchâtel, 11 rue Emile Argand, CP158, 2009 Neuchâtel, Switzerland. Tel.: +41 32 718 26 70; fax: +41 32 718 26 01.
E-mail address: francois.negro@unine.ch (F. Negro).

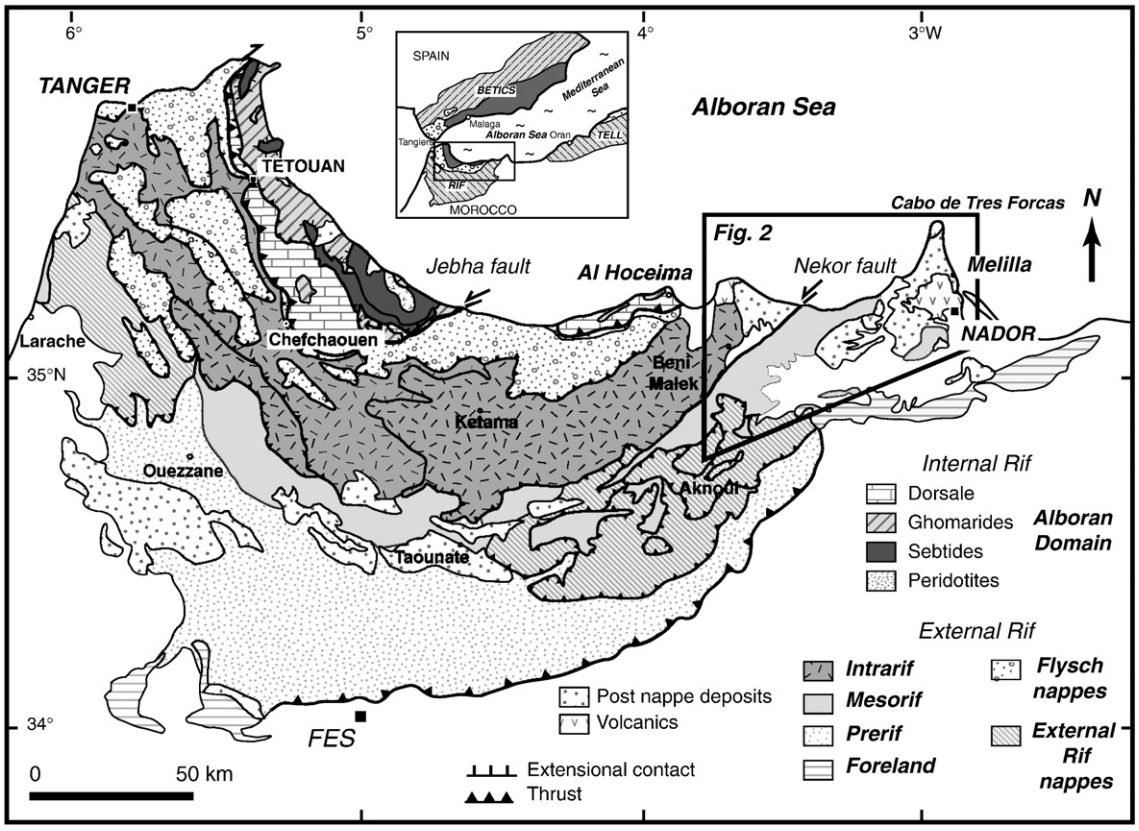

Fig. 1. Geological and tectonic map of the Rif. Modified after Chalouan et al. (2001) and Frizon de Lamotte (1987) for the External Rif.

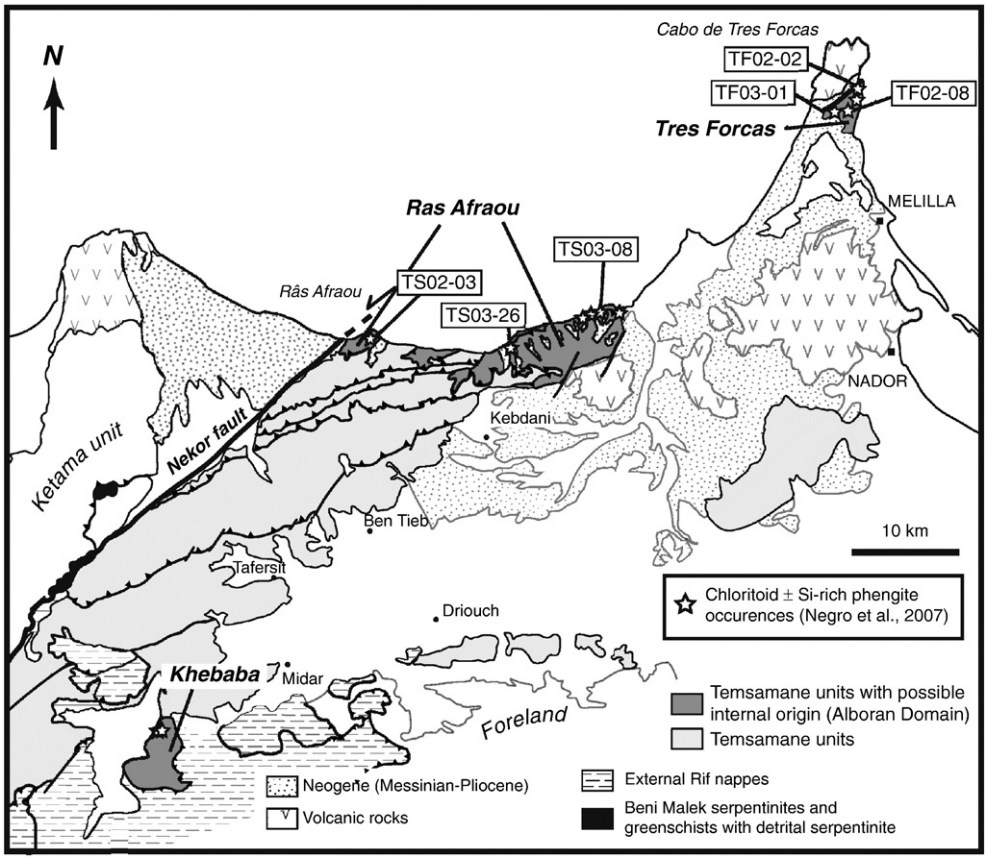

Fig. 2. Geological map of the Temsamane units (modified after Frizon de Lamotte, 1987) showing locations of dated samples by $^{40}Ar/^{39}Ar$ (for location see Fig. 1).

Table 1
Sample description and petrography of the dated samples

Sample	Lithology	Unit	Main mineral assemblage	Si content in white mica	X ray diffraction	Remarks
				Thin sections		
TS02-03	Schist	Ras Afraou	Chlorite–phengite–quartz	3.06–3.32	Illite–kaolinite	Intense deformation
TS03-08	Schist/Vein	Ras Afraou	Chloritoid–phengite–kaolinite	3.03–3.22	Illite–kaolinite–paragonite	Vein/schist interface
TS03–26	Schist	Ras Afraou	Chloritoid–phengite–kaolinite	3.07–3.26	Illite	
TF02-02	Schist	Tres Forcas	Chloritoid–chlorite–phengite	3.02–3.33	Illite–kaolinite–paragonite	Near contact
TF02-08	Schist	Tres Forcas	Chloritoid–chlorite–phengite	3.01–3.38	Illite–kaolinite–paragonite	
TF03-01	Schist	Tres Forcas	Chloritoid–chlorite–phengite–albite	3.03–3.09	Illite	Near contact

Martínez et al., 2002; Negro et al., 2007). As the retrogression was intense, the timing of the early MP–LT event is very challenging.

The aim of this paper is to constrain the timing of this early tectonic and metamorphic event that affected the Temsamane units in order to better assess the dynamics of the Betic–Rif arc.

We present the first $^{40}Ar/^{39}Ar$ dating on the MP–LT Temsamane units, together with a detailed petrological study of the samples. We then compare our results with the available geochronological data in the whole Betic–Rif orogen and discuss the implications for regional geodynamics.

2. Geological setting

The Rif chain, represents the northern part of Morocco. It is classically divided into three geological domains: the External Rif, the Flysch units and the Internal Rif, also known as the Alboran Domain (Fig. 1; Suter, 1980). The External Rif nappe stack is divided into the Prerif, Mesorif and Intrarif domains. The different units of the External Rif are separated by major southward to southwestward-directed thrusts (Fig. 1). Strati-graphic arguments suggested that the main tectonic phase on nappe stacking in the External Rif is Middle to Late Miocene in age (i.e. Frizon de Lamotte et al., 2004). All these units are non-metamorphic or recorded low-grade greenschist facies metamorphism (Andrieux 1973; Frizon de Lamotte, 1985; Azdimousa et al., 1998) but locally MP–LT metamorphic conditions (7–9 kbar; 330–430 °C) were recently discovered in the Temsamane units (Mesorif; Negro et al., 2007).

The Temsamane units (Mesorif) crop out in the eastern part of the Rif, between Al Hoceima and Melilla (Fig.1). This massif is elongated NE–SW and is bounded to the west by Nekor sinistral strike–slip fault, and to the south by the Rif foreland units and the External Rif nappes (Fig. 2). The massif can be divided into 7 distinct tectonic units, bounded by north-dipping thrusts which strike parallel to the length of the massif (Fig. 2). The Ras Afraou, Tres Forcas and Khebaba units could possibly have an internal origin related with Alboran Domain (Fig. 2; Suter 1980, Negro et al., 2007). These three units present similar metamorphic assemblages with chlorite–phengite–quartz ± chloritoid ± kaolinite+ paragonite (Negro et al., 2007). The only geochronological data available on the Temsamane units ($^{40}Ar/^{39}Ar$ dating on micas), range between 28 and 8 Ma (Monié et al.,1984), but were not realized on these units and do not account for the MP–LT metamorphic conditions.

3. Sample description and petrography

The five dated samples belong to the Ras Afraou and Tres Forcas units, their location are reported in Fig. 2. Samples from schist and synfolial quartz veins were selected taking into account (1) the intensity of deformation and (2) the structural position relative to tectonic contacts. Lithological and petrological characteristics of the samples are listed in Table 1 and representative analyses of white micas are given in Table 2. Mineral analyses were performed using Cameca SX50 and SX100 electron microprobes (EMP) (Camparis, University Paris VI) using standard conditions (15 kV, 10 nA) and the

Table 2
Representative electron microprobe analysis of phengite in the dated samples

Sample	TF02-08	TF02-08	TF02-08	TF02-08	TF02-08	TF02-02	TF02-02	TF03-01	TF03-01	TS02-03	TS03-26	TS03-08
Unit	TF	TF	TF	TF	TF	TF	TF	TF	TF	RA	RA	RA
	Sep.	Sep.	Th. Sec.	Th. Sec.	Th. Sec.	Sep.	Th. Sec.	Sep.	Th. Sec.	Th. Sec.	Th. Sec.	Th. Sec.
			Relic	Foliation	Foliation		Foliation		Foliation	Foliation	Foliation	Foliation
SiO_2	49.615	47.163	50.432	48.057	46.867	46.659	46.985	46.784	47.447	47.706	46.880	46.850
TiO_2	0.218	0.039	0.000	0.152	0.135	0.203	0.367	0.199	0.053	0.372	0.212	0.103
Al_2O_3	28.547	38.974	28.712	35.425	36.560	33.726	33.811	35.923	37.380	33.394	32.494	35.168
FeO	2.804	0.429	3.211	1.602	1.028	2.099	2.242	1.443	0.776	1.809	4.658	1.425
MnO	0.024	0.001	0.000	0.000	0.108	0.013	0.015	0.000	0.037	0.000	0.000	0.058
MgO	2.302	0.218	2.283	0.859	0.574	1.091	1.005	0.662	0.443	1.132	0.681	0.738
CaO	0.035	0.080	0.003	0.006	0.022	0.059	0.004	0.022	0.010	0.041	0.011	0.000
Na_2O	0.549	6.797	0.221	0.930	1.159	0.755	1.123	1.335	1.356	0.713	0.735	1.076
K_2O	9.515	1.616	10.058	9.621	8.822	9.104	8.936	9.067	8.911	9.331	9.660	9.130
F	0.000	0.000	0.179	0.257	0.172	0.000	0.000	0.000	0.120	0.000	0.323	0.128
Total	93.619	95.325	95.104	96.908	95.449	93.710	94.507	95.453	96.534	94.497	95.683	94.696
Structural formula												
Si	3.359	3.022	3.376	3.135	3.084	3.144	3.142	3.088	3.081	3.183	3.158	3.119
Ti	0.011	0.002	0.000	0.007	0.007	0.010	0.018	0.010	0.003	0.019	0.011	0.005
Al	2.278	2.943	2.265	2.723	2.836	2.678	2.665	2.794	2.861	2.625	2.579	2.759
Fe^{2+}	0.159	0.023	0.180	0.087	0.057	0.118	0.125	0.080	0.042	0.101	0.262	0.079
Mn	0.001	0.000	0.000	0.000	0.006	0.001	0.001	0.000	0.002	0.000	0.000	0.003
Mg	0.232	0.021	0.228	0.084	0.056	0.110	0.100	0.065	0.043	0.113	0.068	0.073
Ca	0.003	0.005	0.000	0.000	0.002	0.004	0.000	0.002	0.001	0.003	0.001	0.000
Na	0.072	0.844	0.029	0.118	0.148	0.099	0.146	0.171	0.171	0.092	0.096	0.139
K	0.822	0.132	0.859	0.801	0.741	0.783	0.762	0.763	0.738	0.794	0.830	0.775
F	0.000	0.000	0.038	0.053	0.036	0.000	0.000	0.002	0.025	0.000	0.069	0.027
Sum.	6.924	6.967	6.974	7.006	6.971	6.879	6.963	6.936	6.965	6.929	7.077	6.983

RA: Ras Afraou; TF: Tres Forcas; Sep.: mica separate; Th. Sec.: thin section.

following standards: Fe_2O_3 (Fe), $MnTiO_3$ (Mn, Ti), diopside (Mg, Si, Ca), orthoclase (Al, K), albite (Na) and CaF_2 (F). XRD analyses were also performed on all the samples (Table 1).

3.1. Ras Afraou unit

3.1.1. Sample TS02–03

This sample was collected in the Ras Afraou area near the Nekor fault (Fig. 2). This area is characterized by an intense E–W stretching (Negro et al., 2007), that strongly affected the schist. The main foliation S_2 is beared by chlorite–phengite–quartz assemblage (Fig. 3a). Chloritoid is not preserved in this part of the Ras Afraou unit. White micas display variable compositions, depending on whether they lie in the foliation or in S–C shear bands. The Si concentrations (expressed as atoms per formula units, a.p.f.u) range between 3.06 and 3.32 (Tables 1 and 2).

3.1.2. Sample TS03–26

This sample was collected further east, north of Kebdani (Fig. 2). It is a schist sample characterized by a penetrative S_2 foliation,

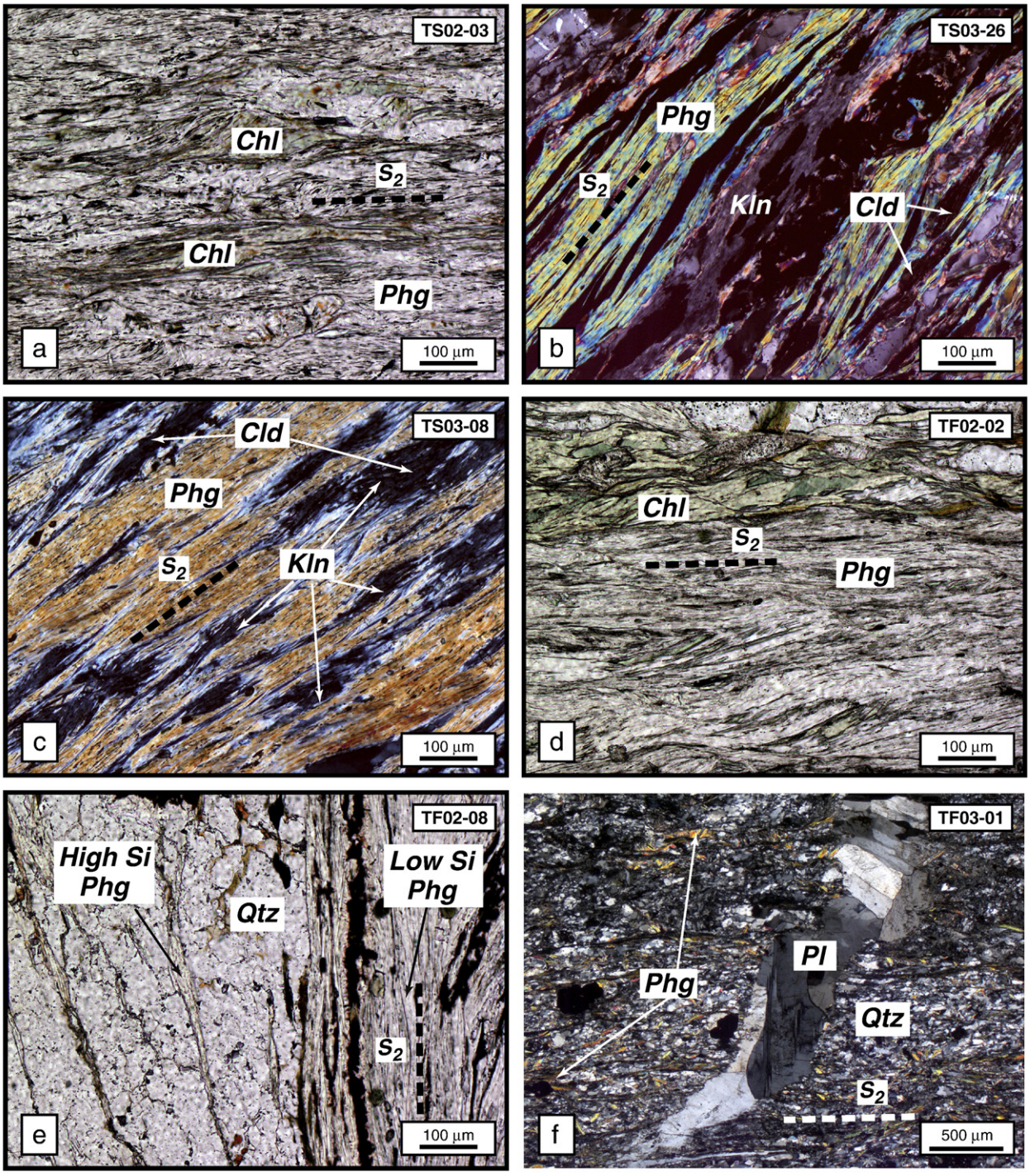

Fig. 3. Microphotographs depicting the mineralogy of the dated samples. Samples are located in Fig. 2. (a) Chlorite–phengite S_2 foliation in the TS-02-03 sample (plane polarized light). (b) Phengite–kaolinite S_2 folation in the TS03-26 sample (crossed polars). (c) Phengite–kaolinite S_2 foliation in the TS03-08 sample (crossed polars). (d) Chlorite–phengite S_2 foliation in the TF02-02 sample (plane polarized light). (e) Chemical variability of phengite in the TF02-08 sample (plane polarized light). (f) Quartz–phengite S_2 foliation cross-cut by late plagioclase vein in the TF03-01 samples (crossed polars).

underlined by chloritoid, phengite and kaolinite (Fig. 3b). The Si concentrations show slightly less disequilibrium than the previous sample and range between 3.07 and 3.26 (Tables 1 and 2).

3.1.3. Sample TS03-08

This sample was collected east of TS03-26 (Fig. 2). Sample TS03-08 corresponds to the interface between schist and a synfolial quartz vein. The main foliation (S_2) is characterized by phengite+kaolinite ±chloritoid (Fig. 3c). Furthermore, this sample shows important retrogression as illustrated by the replacement of chloritoid by kaolinite (Negro et al., 2007). White micas show Si concentrations in the range 3.03–3.22, the higher Si values corresponding to the white micas located in the quartz vein (Tables 1 and 2).

3.2. Tres Forcas unit

3.2.1. Sample TF02-02

This sample was collected north of the Tres Forcas unit, near the normal fault which marks the limit with Tortonian–Messinian sediments to the north. This part of the unit is affected by intense ductile deformation and late brittle deformation. The sample is characterized by a penetrative chlorite–phengite S_2 foliation (Fig. 3d).

3.2.2. Sample TF02-08

This sample was collected south of TF02-02, in the core of the Tres Forcas unit. In this sample two mica generations are observed: micas with high celadonite content (Si up to 3.4 a.p.f.u) are preserved as inclusion in quartz veins whereas lower Si concentrations (3–3.2 a.p.f.u) characterize micas underlining the S_2 foliation (Fig. 3e). Furthermore mica separates from sample TF02-08 show chemical zoning at mineral scale when observed with Back Scattered Electron (BSE) (Fig. 4a) with two types of tightly intergrown micas: one corresponding to high-Si content (ca. 3.35 a.p.f.u) and one corresponding to low-Si content (ca. 3.05 a.p.f.u) (Fig. 4b and Table 2). Therefore, the mica separates reflects the two micas generation observed in thin sections (Fig. 3e and Table 2). Furthermore, the low-Si mica generation has similar composi-tions to TF02-02 (Fig. 4b and Table 2).

3.2.3. Sample TF03-01

This sample was collected southwest of TF02-02, and is also affected by intense retrogression and late brittle deformation. The sample is characterized by a phengite–quartz S_2 foliation, which is cross-cut by late albite veins (Fig. 3e). Low-Si mica generation underlining the foliation has also similar composition to TF02-02 (Fig. 4b and Table 2).

In summary, the combination of XRD and EMP demonstrates that in all samples kaolinitization was a major process (Tables 1 and 2). Most samples contain significant amounts of phengitic (high-Si) relics; paragonite was also observed in most samples (Table 1). This strong, ubiquitous mineralogical heterogeneity is best explained by the low-grade metamorphic conditions that were insufficient for pervasive recrystallization.

4. $^{40}Ar/^{39}Ar$ dating

4.1. Analytical techniques

Samples were crushed and sieved, and micas having diameters between 100–125 μm were separated by magnetic and gravimetric means. About 10–20 mg was further purified by hand-picking under a binocular microscope. The mica separates were analysed by XRD (Table 1) and were mounted in epoxy resin, observed in back-scattered mode and analysed by EMP. Samples were irradiated at the TRIGA (Pavia, Italy) and McMaster (Canada) reactors. Analyses were performed in a double-vacuum resistance oven connected to a MAP 215-50B spectrometer (University of Bern) following the procedure

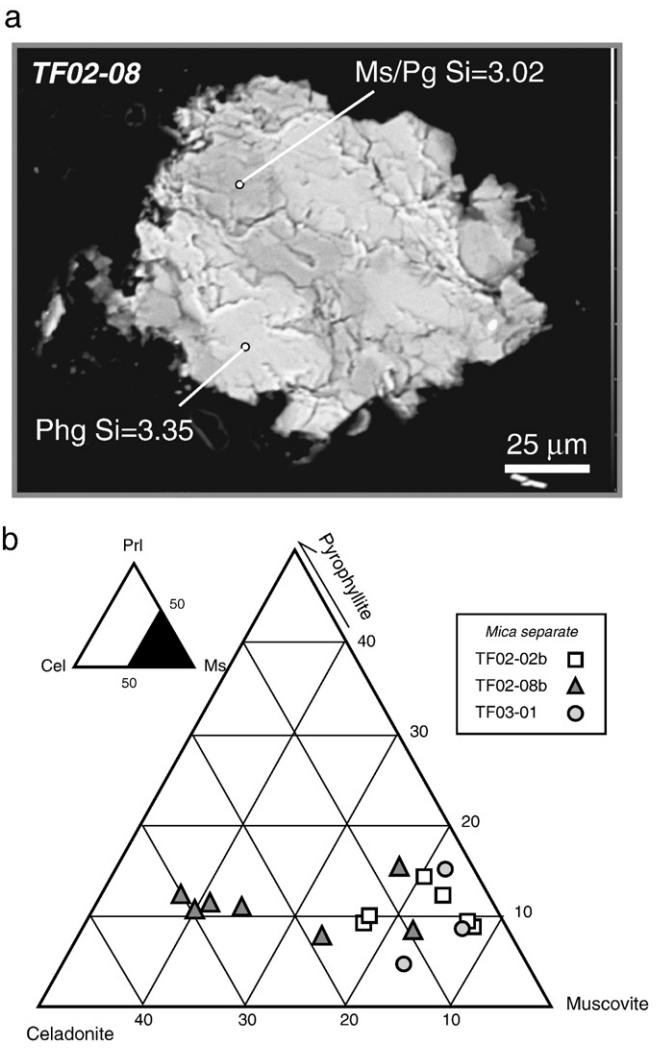

Fig. 4. (a) EMP back-scattered electron image of mica from sample TF02-08. (b) Celadonite–Muscovite–Pyrophyllite ternary diagrams of phengite compositions of TF02-02, TF02-08 and TF03-01 mica separates.

described in Villa et al. (2000). Results of $^{40}Ar/^{39}Ar$ analyses are listed in Table 3. Ever since the beginnings of the Ar^{40}/Ar^{39} technique, natural samples that display discordant age spectra have been successfully interpreted in terms of complex geological histories (e.g. Merrihue and Turner, 1966). In the subsequent four decades, increasing understanding of the connections between microstructures, microchemistry, and the isotope record have improved our ability to accurately interpret such discordant age spectra (e.g. Müller et al., 2002). A decisive role is played by the chemical indications provided by the $^{38}Ar/^{39}Ar$ and $^{37}Ar/^{39}Ar$ ratios, which mirror the Cl/K and Ca/K ratios, respectively (e.g. Kelley et al., 1986).

The Cl/K and Ca/K ratios derived from each step of heating allow distinguishing different phases or different mica population in a dated sample (Villa et al., 1997, 2000). Therefore internally discordant age spectra can be interpreted as mineral mixtures, provided these are documented petrographically (Villa, 2001). This has been demonstrated for the case of a magmatic–hydrothermal phengite mixture (Villa et al., 1997) or multiples zoned amphibole generations (Villa et al., 2000). Moreover, this approach allows distinguish between Ar loss from a homogeneous population of mica grains (in which case the apparent step ages vary while the Cl/K and Ca/K ratios both stay constant), or coexistence of diachronic and heterochemical mica generations (in which case there is a covariation, positive or negative,

Table 3
$^{40}Ar/^{39}Ar$ data

T (°C)	^{40}Ar total	Error ^{40}Ar	^{40}Ar*	^{39}Ar	Error ^{39}Ar	%^{39}Ar	^{38}Ar	Error ^{38}Ar	(^{38}Ar)Cl	^{37}Ar	Error ^{37}Ar	^{36}Ar	Error ^{36}Ar	Age	Error age	Ca/K	Cl/K	Ca/Cl
J=0.00233																		
TS02-03 (20.3 mg)																		
585	1.44E−08	1.40E−10	8.76E−12	1.54E−10	4.30E−12	2.01	1.97E−11	8.00E−13	8.80E−12	2.69E−12	3.08E−12	4.87E−11	3.30E−13	0.24	2.65	3.39E−02	1.31E−02	2.6
698	5.98E−09	9.40E−11	4.84E−09	6.52E−10	1.30E−11	8.51	1.05E−11	7.60E−13	2.07E−12	−1.20E−11	−2.12E−12	3.84E−12	2.90E−13	30.94	0.97	−3.56E−02	7.31E−04	−48.8
791	1.22E−08	7.50E−11	1.48E−09	2.38E−09	6.00E−12	31.00	6.99E−11	1.40E−12	3.51E−11	6.27E−11	2.26E−12	3.63E−11	4.70E−13	2.62	0.24	5.12E−02	3.40E−03	15.1
852	1.10E−08	5.40E−11	3.30E−09	1.42E−09	7.40E−12	18.55	3.05E−11	3.40E−13	8.87E−12	1.12E−11	4.34E−13	2.62E−11	4.10E−13	9.74	0.36	1.52E−02	1.43E−03	10.6
892	8.55E−09	1.00E−11	1.66E−09	7.33E−10	6.60E−13	9.56	1.77E−11	2.40E−13	4.72E−12	7.64E−12	5.50E−13	2.33E−11	3.70E−13	9.49	0.63	2.02E−02	1.48E−03	13.6
950	9.98E−09	5.60E−12	2.38E−09	8.02E−10	2.10E−12	10.46	1.66E−11	1.50E−13	2.37E−12	4.05E−12	7.22E−13	2.57E−11	3.20E−13	12.43	0.51	9.79E−03	6.79E−04	14.4
1063	1.07E−08	2.10E−11	4.00E−09	1.35E−09	1.30E−12	17.64	2.48E−11	2.70E−13	4.66E−12	6.02E−12	3.85E−13	2.28E−11	3.40E−13	12.38	0.31	8.64E−03	7.92E−04	10.9
1325	5.76E−09	9.50E−12	2.76E−10	1.73E−10	7.90E−13	2.26	6.26E−12	2.50E−13	7.63E−13	8.64E−12	3.03E−13	1.86E−11	3.30E−13	6.70	2.34	9.69E−02	1.02E−03	95.5
Total (ml)			1.80E−08	7.67E−09					6.74E−11	9.10E−11		2.05E−10		9.82		2.30E−02	2.02E−03	11.4
Total (ml/g)			1.49E−06	6.38E−07								1.71E−08						
Concentration (g/g)				3.92E−02														
TS03-08 (19.7 mg)																		
584	1.26E−08	5.90E−11	2.33E−09	3.69E−10	2.40E−12	8.07	3.75E−11	2.90E−13	2.67E−11	5.36E−11	6.46E−13	3.47E−11	3.10E−13	26.36	1.06	2.81E−01	1.66E−02	16.9
695	1.66E−08	1.50E−10	1.41E−09	1.02E−09	1.40E−12	22.27	3.97E−11	8.20E−13	1.81E−11	4.42E−11	1.58E−12	5.14E−11	5.40E−13	5.80	0.65	8.42E−02	4.08E−03	20.6
786	1.97E−08	7.30E−11	2.12E−09	1.40E−09	3.30E−12	30.51	5.32E−11	4.80E−13	2.56E−11	4.93E−11	6.91E−13	5.96E−11	4.50E−13	6.36	0.41	6.84E−02	4.21E−03	16.2
843	1.73E−08	6.00E−11	3.20E−09	6.13E−10	1.80E−12	13.39	2.07E−11	2.70E−13	4.56E−12	1.01E−11	3.98E−13	4.79E−11	3.90E−13	21.80	0.79	3.21E−02	1.71E−03	18.7
888	1.89E−08	2.10E−12	1.63E−09	3.90E−10	8.80E−13	8.51	1.73E−11	2.00E−13	1.74E−12	2.40E−12	3.51E−13	5.86E−11	3.80E−13	17.50	1.20	1.19E−02	1.03E−03	11.6
945	1.61E−08	1.80E−11	2.34E−09	2.97E−10	6.10E−13	6.49	1.34E−11	1.70E−13	1.22E−12	1.83E−13	−4.76E−13	4.67E−11	3.50E−13	32.83	1.45	1.20E−03	9.44E−04	1.3
1324	1.54E−08	4.50E−11	3.52E−09	4.93E−10	1.00E−12	10.76	1.56E−11	2.40E−13	2.26E−12	2.07E−11	5.91E−13	4.03E−11	4.80E−13	29.74	1.20	8.13E−02	1.06E−03	77.0
Total (ml)			1.65E−08	4.58E−09					8.02E−11	1.80E−10		3.39E−10		15.13		7.65E−02	4.03E−03	19.0
Total (ml/g)			1.42E−06	3.93E−07								2.91E−08						
Concentration (g/g)				2.41E−02														
TS03-26 (20.1 mg)																		
588	3.11E−09	2.00E−12	−1.40E−09	1.84E−10	2.60E−12	3.81	2.21E−11	1.30E−12	1.71E−11	2.47E−11	2.95E−12	1.53E−11	4.40E−13	−32.10	−2.90	2.60E−01	2.13E−02	12.2
701	1.12E−09	2.80E−11	−6.34E−10	2.90E−10	5.80E−12	5.99	7.52E−12	1.70E−12	3.00E−12	2.25E−11	4.06E−12	5.95E−12	1.00E−12	−9.22	−4.35	1.51E−01	2.38E−03	63.3
793	8.40E−09	1.90E−11	7.96E−10	1.57E−09	1.20E−11	32.40	4.62E−11	1.30E−13	2.30E−11	3.92E−11	3.53E−13	2.57E−11	3.70E−13	2.13	0.29	4.85E−02	3.37E−03	14.4
854	6.41E−09	4.10E−11	1.09E−09	6.32E−10	2.60E−12	13.05	2.02E−11	3.90E−13	9.44E−12	1.72E−11	6.00E−13	1.80E−11	3.70E−13	7.23	0.72	5.27E−02	3.44E−03	15.3
892	4.93E−09	1.10E−11	9.84E−10	3.99E−10	1.20E−12	8.24	8.13E−12	2.00E−13	9.46E−13	4.26E−12	6.58E−13	1.34E−11	3.50E−13	10.35	1.09	2.07E−02	5.46E−04	38.0
944	5.15E−09	7.50E−12	1.21E−09	5.26E−10	1.40E−12	10.88	1.13E−11	2.00E−13	2.66E−12	2.85E−12	3.68E−13	1.33E−11	4.00E−13	9.63	0.94	1.05E−02	1.16E−03	9.0
1059	7.16E−09	1.80E−11	3.99E−09	1.18E−09	3.40E−12	24.31	1.87E−11	3.90E−13	2.83E−12	2.51E−12	5.71E−13	1.07E−11	3.20E−13	14.21	0.34	4.14E−03	5.54E−04	7.5
1319	3.14E−09	9.50E−12	7.69E−10	6.43E−11	2.00E−13	1.33	4.12E−12	2.00E−13	1.86E−12	4.37E−12	3.53E−13	8.02E−12	3.00E−13	49.59	5.55	1.32E−01	6.67E−03	19.8
Total (ml)			6.81E−09	4.84E−09					6.08E−11	1.18E−10		1.10E−10		8.49		4.71E−02	2.89E−03	16.3
Total (ml/g)			5.73E−07	4.07E−07								9.28E−09						
Concentration (g/g)				2.50E−02														
TF02-02a (19.5 mg)																		
583	1.11E−08	1.30E−10	1.98E−09	2.12E−10	4.00E−12	2.94	2.26E−11	1.20E−12	1.44E−11	2.54E−11	9.10E−13	3.10E−11	3.10E−13	38.85	1.98	2.32E−01	1.56E−02	14.9
699	9.03E−09	6.70E−11	9.66E−10	1.10E−09	3.00E−12	15.29	6.68E−11	3.70E−13	4.87E−11	8.22E−11	9.36E−13	2.73E−11	3.00E−13	3.68	0.34	1.45E−01	1.02E−02	14.2
790	8.23E−09	1.80E−12	1.06E−09	1.44E−09	2.20E−12	20.00	5.12E−11	1.10E−13	2.97E−11	4.62E−11	1.59E−12	2.43E−11	3.10E−13	3.10	0.27	6.22E−02	4.74E−03	13.1
848	6.77E−09	2.80E−12	2.25E−09	8.53E−10	8.30E−13	11.84	2.03E−11	2.30E−13	7.37E−12	6.38E−12	4.26E−13	1.53E−11	3.00E−13	11.06	0.43	1.45E−02	1.99E−03	7.3
895	7.76E−09	4.10E−12	3.03E−09	9.92E−10	1.10E−12	13.77	2.09E−11	1.10E−13	6.22E−12	3.00E−12	3.87E−13	1.60E−11	3.50E−13	12.78	0.43	5.87E−03	1.44E−03	4.1
950	6.81E−09	2.60E−12	2.50E−09	7.90E−10	8.80E−13	10.97	1.72E−11	1.80E−13	5.13E−12	4.54E−12	3.63E−13	1.46E−11	3.20E−13	13.25	0.51	1.11E−02	1.49E−03	7.5
1064	9.56E−09	5.80E−12	5.06E−09	1.59E−09	1.70E−12	22.13	2.66E−11	1.60E−13	5.05E−12	1.04E−11	1.20E−13	1.52E−11	3.50E−13	13.29	0.27	1.26E−02	7.29E−04	17.4
1322	4.68E−09	1.70E−12	5.83E−10	2.21E−10	2.40E−13	3.06	1.12E−11	1.60E−13	5.98E−12	1.76E−11	5.74E−13	1.39E−11	3.20E−13	11.06	1.81	1.55E−01	6.23E−03	24.8
Total (ml)			1.74E−08	7.20E−09					1.23E−10	1.96E−10		1.58E−10		10.14		5.27E−02	3.91E−03	13.5
Total (ml/g)			1.51E−06	6.24E−07								1.37E−08						
Concentration (g/g)				3.83E−02														
TF02-08a (16.5 mg)																		
589	6.81E−09	5.80E−11	1.61E−09	2.24E−10	2.00E−12	3.62	1.96E−11	4.60E−13	1.36E−11	2.41E−11	1.46E−12	1.76E−11	2.90E−13	29.93	1.64	2.09E−01	1.40E−02	14.9
702	1.12E−08	7.10E−11	3.31E−10	8.59E−10	8.30E−12	13.88	4.28E−11	5.40E−13	2.58E−11	5.13E−11	1.76E−12	3.69E−11	3.10E−13	1.62	0.46	1.16E−01	6.92E−03	16.8
792	1.42E−08	3.70E−11	1.91E−09	1.20E−09	3.90E−12	19.47	4.14E−11	5.10E−13	1.94E−11	3.14E−11	6.62E−13	4.18E−11	5.20E−13	6.65	0.53	5.05E−02	3.71E−03	13.6
854	1.69E−08	6.10E−12	4.18E−09	1.25E−09	4.00E−12	20.27	2.73E−11	2.50E−13	4.48E−12	−9.65E−13	−3.01E−13	4.30E−11	3.70E−13	13.94	0.36	−1.49E−03	8.22E−04	−1.8
890	1.50E−08	2.20E−11	3.47E−09	8.72E−10	2.40E−12	14.10	2.18E−11	1.80E−13	4.22E−12	5.40E−12	3.14E−13	3.91E−11	3.30E−13	16.63	0.48	1.20E−02	1.11E−03	10.8

944	1.22E−08	7.50E−11	2.79E−09	6.88E−10	3.40E−12	11.12	1.65E−11	1.70E−13	2.47E−12	1.61E−12	2.99E−13	3.18E−11	3.70E−13	16.95	0.68	4.54E−03	8.26E−04	5.5
1058	1.10E−08	1.90E−11	3.03E−09	8.91E−10	1.80E−12	14.40	1.89E−11	1.60E−13	3.38E−12	2.50E−12	4.14E−13	2.69E−11	3.30E−13	14.22	0.46	5.44E−03	8.72E−04	6.2
1323	7.41E−09	1.60E−11	5.73E−10	1.95E−10	6.70E−13	3.15	1.07E−11	1.40E−13	4.08E−12	3.15E−12	4.67E−13	2.31E−11	3.10E−13	12.33	1.95	3.14E−02	4.83E−03	6.5
Total (ml)			1.79E−08	6.19E−09					7.75E−11	1.18E−10		2.60E−10		12.11		3.71E−02	2.88E−03	12.9
Total (ml/g)			1.83E−06	6.34E−07								2.67E−08				0.00E+00		
Concentration (g/g)				3.89E−02												0.00E+00		
J=0.000585																		
TF02-02b (8.6 mg)																		
482	6.24E−09	2.20E−10	1.82E−09	6.24E−11	5.40E−13	5.11	1.12E−11	1.10E−12	7.65E−12	2.45E−12	6.87E−13	1.50E−11	9.40E−13	30.50	4.80	7.60E−02	2.82E−02	2.7
562	4.63E−09	2.10E−10	1.59E−09	6.80E−11	2.90E−12	5.56	2.39E−12	1.40E−12	−3.35E−13	6.56E−13	7.14E−13	1.03E−11	7.10E−14	24.49	1.50	1.87E−02	−1.13E−03	−16.5
602	1.10E−09	2.60E−11	−7.24E−11	1.40E−11	2.30E−13	1.15	4.50E−12	1.40E−13	3.59E−12	5.18E−12	5.74E−13	3.97E−12	8.50E−14	−5.47	−1.90	7.18E−01	5.90E−02	12.2
671	1.75E−09	6.70E−11	5.03E−10	4.02E−11	7.10E−13	3.29	1.51E−11	2.10E−13	1.38E−11	9.91E−12	5.43E−13	4.22E−12	9.60E−14	13.16	0.92	4.78E−01	7.90E−02	6.1
729	1.56E−09	3.60E−11	5.00E−10	4.11E−11	2.10E−13	3.36	6.27E−12	2.00E−13	5.12E−12	2.81E−12	5.96E−13	3.60E−12	6.20E−13	12.81	4.70	1.32E−01	2.86E−02	4.6
781	7.25E−10	8.90E−12	7.94E−11	3.57E−11	2.50E−13	2.92	2.58E−12	1.40E−13	1.75E−12	2.43E−12	4.46E−13	2.19E−12	2.20E−13	2.35	1.90	1.32E−01	1.13E−02	11.7
831	5.73E−10	2.60E−12	2.39E−10	3.43E−11	1.40E−13	2.80	1.79E−13	2.00E−13	−4.36E−13	1.33E−12	4.28E−13	1.13E−12	1.60E−13	7.35	1.50	7.55E−02	−2.92E−03	−25.8
878	1.01E−09	1.60E−12	6.81E−10	6.70E−11	2.30E−13	5.48	2.62E−12	1.40E−13	1.62E−12	7.88E−14	−6.37E−13	1.11E−12	9.50E−14	10.70	0.44	2.28E−03	5.58E−03	0.4
909	8.41E−09	2.10E−12	7.05E−09	6.02E−10	6.60E−13	49.22	9.51E−12	2.50E−13	1.57E−12	9.45E−14	7.22E−13	4.60E−12	1.40E−13	12.33	0.07	3.05E−04	6.02E−04	0.5
942	1.76E−09	6.20E−13	1.37E−09	1.14E−10	1.80E−13	9.30	1.70E−12	1.60E−13	1.16E−13	1.16E−12	3.64E−13	1.32E−12	1.10E−13	12.71	0.29	1.98E−02	2.35E−04	84.2
1003	1.07E−09	3.40E−13	6.92E−10	6.93E−11	1.10E−13	5.67	1.52E−12	2.70E−13	4.68E−13	4.23E−13	2.84E−13	1.28E−12	1.60E−13	10.51	0.73	1.18E−02	1.55E−03	7.6
1126	1.16E−09	9.90E−13	7.50E−10	7.17E−11	1.80E−13	5.87	1.10E−12	1.80E−13	−7.82E−16	7.02E−13	5.38E−13	1.39E−12	1.30E−13	11.00	0.57	1.90E−02	−2.51E−06	−7568.7
1397	4.03E−10	7.90E−13	2.27E−10	3.37E−12	3.00E−13	0.28	7.13E−13	1.70E−13	5.62E−13	2.28E−12	4.04E−13	5.96E−13	1.40E−13	69.94	14.00	1.31E+00	3.84E−02	34.2
Total (ml)			1.54E−08	1.22E−09					3.55E−11	2.93E−11		5.06E−11		13.27		4.66E−02	6.68E−03	7.0
Total (ml/g)			3.03E−06	2.40E−07								9.95E−09						
Concentration (g/g)				5.87E−02														
TF02-08b (11.2 mg)																		
480	2.27E−08	2.70E−10	6.12E−09	2.43E−10	3.20E−12	22.23	2.90E−11	6.90E−14	1.56E−11	4.66E−11	1.46E−12	5.62E−11	1.40E−12	26.34	1.90	3.71E−01	1.47E−02	25.2
609	1.81E−09	1.40E−12	9.21E−10	8.76E−11	1.50E−13	8.00	1.91E−12	1.30E−13	3.15E−13	7.99E−13	7.45E−13	3.00E−12	1.10E−13	11.06	0.39	1.77E−02	8.26E−04	21.4
730	5.43E−09	9.70E−12	2.89E−09	2.30E−10	2.50E−13	21.03	5.92E−12	1.40E−13	1.60E−12	5.92E−12	3.69E−13	8.59E−12	2.40E−13	13.20	0.32	4.99E−02	1.60E−03	31.2
756	1.98E−09	9.80E−13	1.55E−09	9.10E−11	1.80E−13	8.30	2.36E−12	2.60E−13	1.02E−12	1.97E−13	2.64E−13	1.44E−12	1.70E−13	17.90	0.57	4.21E−03	2.57E−03	1.6
780	1.44E−09	5.00E−13	1.19E−09	6.25E−11	1.70E−13	5.71	1.91E−12	1.20E−13	1.01E−12	7.73E−13	2.22E−13	8.42E−13	1.40E−13	19.97	0.68	2.40E−02	3.73E−03	6.4
830	1.63E−09	5.30E−13	1.22E−09	6.48E−11	2.40E−13	5.91	7.09E−13	1.70E−13	−3.10E−13	1.15E−15	2.72E−13	1.38E−12	1.90E−13	19.77	0.91	3.43E−05	−1.10E−03	0.0
875	1.70E−09	7.50E−13	1.58E−09	7.20E−11	2.90E−13	6.57	1.15E−12	1.80E−13	2.23E−13	5.62E−13	2.09E−13	4.26E−13	1.40E−13	22.97	0.61	1.52E−02	7.13E−04	21.3
941	1.89E−09	1.40E−12	1.64E−09	9.23E−11	2.00E−13	8.43	2.68E−14	1.30E−13	−1.22E−12	4.35E−13	2.40E−13	8.57E−13	1.40E−13	18.61	0.48	9.15E−03	−3.04E−03	−3.0
1119	2.42E−09	5.90E−13	1.74E−09	1.32E−10	2.00E−13	12.02	2.81E−12	2.10E−13	8.26E−13	3.07E−12	2.57E−13	2.32E−12	1.10E−13	13.87	0.26	4.52E−02	1.44E−03	31.3
1389	1.04E−09	1.90E−14	−2.62E−11	1.48E−11	1.60E−13	1.35	2.44E−13	1.70E−13	−6.06E−13	3.77E−13	2.44E−13	3.62E−12	1.00E−13	−1.87	−2.10	4.94E−02	−9.42E−03	−5.2
Total (ml)			1.88E−08	1.10E−09					1.83E−11	5.94E−11		7.99E−11		17.98		1.05E−01	3.83E−03	27.4
Total (ml/g)			3.28E−06	1.92E−07								1.40E−08						
Concentration (g/g)				4.69E−02														
TF03-01 (6.1 mg)																		
481	8.82E−09	2.90E−10	2.11E−09	7.37E−11	1.90E−12	7.92E+00	2.69E−11	1.30E−12	2.18E−11	4.80E−11	1.25E−12	2.27E−11	9.30E−13	2.99E+01	4.10E+00	1.26E+00	6.80E−02	1.86E+01
557	6.26E−09	2.40E−10	2.23E−09	8.53E−11	1.50E−12	9.17E+00	7.45E−12	5.50E−13	3.90E−12	1.79E−12	1.28E−12	1.36E−11	8.60E−13	2.74E+01	3.30E+00	4.07E−02	1.05E−02	3.88E+00
595	2.04E−09	6.60E−11	6.71E−10	3.12E−11	4.40E−13	3.35E+00	5.95E−12	1.20E−14	4.72E−12	1.03E−11	4.52E−13	4.62E−12	9.70E−14	2.26E+01	1.20E+00	6.39E−01	3.48E−02	1.84E+01
668	1.38E−09	3.70E−11	2.13E−10	2.26E−11	3.10E−13	2.43E+00	7.28E−12	2.40E−13	6.28E−12	4.28E−12	3.28E−13	3.96E−12	3.60E−14	9.92E+00	5.80E−01	3.67E−01	6.38E−02	5.76E+00
732	1.30E−09	3.00E−11	2.24E−10	3.32E−11	1.50E−13	3.56E+00	7.62E−12	2.20E−13	6.55E−12	8.02E−12	6.47E−13	3.64E−12	5.50E−13	7.12E+00	5.20E+00	4.69E−01	4.54E−02	1.03E+01
757	7.08E−10	9.10E−12	−3.65E−10	2.39E−11	2.60E−13	2.57E+00	2.71E−12	1.50E−13	1.75E−12	9.01E−13	4.90E−13	3.63E−12	2.30E−13	−1.62E+01	−3.10E+00	7.32E−02	1.68E−02	4.35E+00
783	6.82E−10	1.70E−11	−1.95E−10	2.45E−11	1.50E−13	2.63E+00	2.49E−12	1.40E−13	1.65E−12	−9.99E−14	−3.18E−13	2.97E−12	1.50E−13	−8.43E+00	−1.90E+00	−7.93E−03	1.55E−02	−5.12E−01
783	6.96E−10	1.50E−11	1.35E−11	2.14E−11	2.80E−13	2.30E+00	3.96E−12	1.70E−13	3.28E−12	2.98E−12	4.28E−13	2.31E−12	9.70E−14	6.66E−01	1.40E+00	2.70E−01	3.52E−02	7.67E+00
831	5.73E−10	9.80E−12	−3.40E−10	1.85E−11	1.30E−13	1.99E+00	2.03E−12	1.40E−13	1.23E−12	2.90E−12	5.45E−13	3.09E−12	2.60E−13	−1.95E+01	−4.40E+00	3.05E−01	1.53E−02	1.99E+01
878	6.81E−10	7.20E−12	−1.28E−10	3.14E−11	8.20E−14	3.38E+00	2.43E−12	1.70E−13	1.55E−12	2.94E−12	3.14E−13	2.74E−12	1.40E−13	−4.30E+00	−1.40E+00	1.82E−01	1.13E−02	1.61E+01
909	6.76E−09	5.80E−13	5.56E−09	4.32E−10	5.10E−13	4.65E+01	7.65E−12	2.10E−13	1.80E−12	−1.44E−14	−6.48E−13	4.08E−12	9.70E−14	1.35E+01	7.10E−02	3.00E−03	9.61E−04	3.12E+00
940	9.34E−10	7.70E−13	5.08E−10	5.37E−11	1.80E−13	5.78E+00	2.22E−12	2.10E−13	1.32E−12	3.23E−12	4.03E−13	1.44E−12	1.50E−13	9.96E+00	8.90E−01	1.17E−01	5.65E−03	2.07E+01
999	6.76E−10	5.00E−13	3.38E−10	3.57E−11	2.20E−13	3.83E+00	2.00E−12	2.30E−13	1.36E−12	4.83E−13	5.53E−13	1.14E−12	1.40E−13	9.99E+00	1.20E+00	2.63E−02	8.79E−03	2.99E+00
1126	7.31E−10	5.20E−13	3.06E−10	3.91E−11	1.40E−13	4.21E+00	1.32E−12	2.50E−13	5.94E−13	6.90E−13	3.72E−13	1.44E−12	1.40E−13	8.23E+00	1.10E+00	3.42E−02	3.49E−03	9.80E+00
1401	3.62E−10	5.50E−13	−1.44E−10	4.00E−12	2.60E−13	4.30E−01	4.19E−14	7.90E−14	−3.25E−13	1.44E−12	5.19E−13	1.71E−12	1.10E−13	−3.84E+01	−9.50E+00	7.00E−01	−1.87E−02	−3.74E+01
Total (ml)			1.10E−08	9.30E−10					5.74E−11	8.78E−11		7.31E−11		1.24E+01		1.83E−01	1.42E−02	1.29E+01
Total (ml/g)			3.05E−06	2.58E−07								2.03E−08						
Concentration (g/g)				6.30E−02														

Absolute errors are given at the 1σ confidence level.

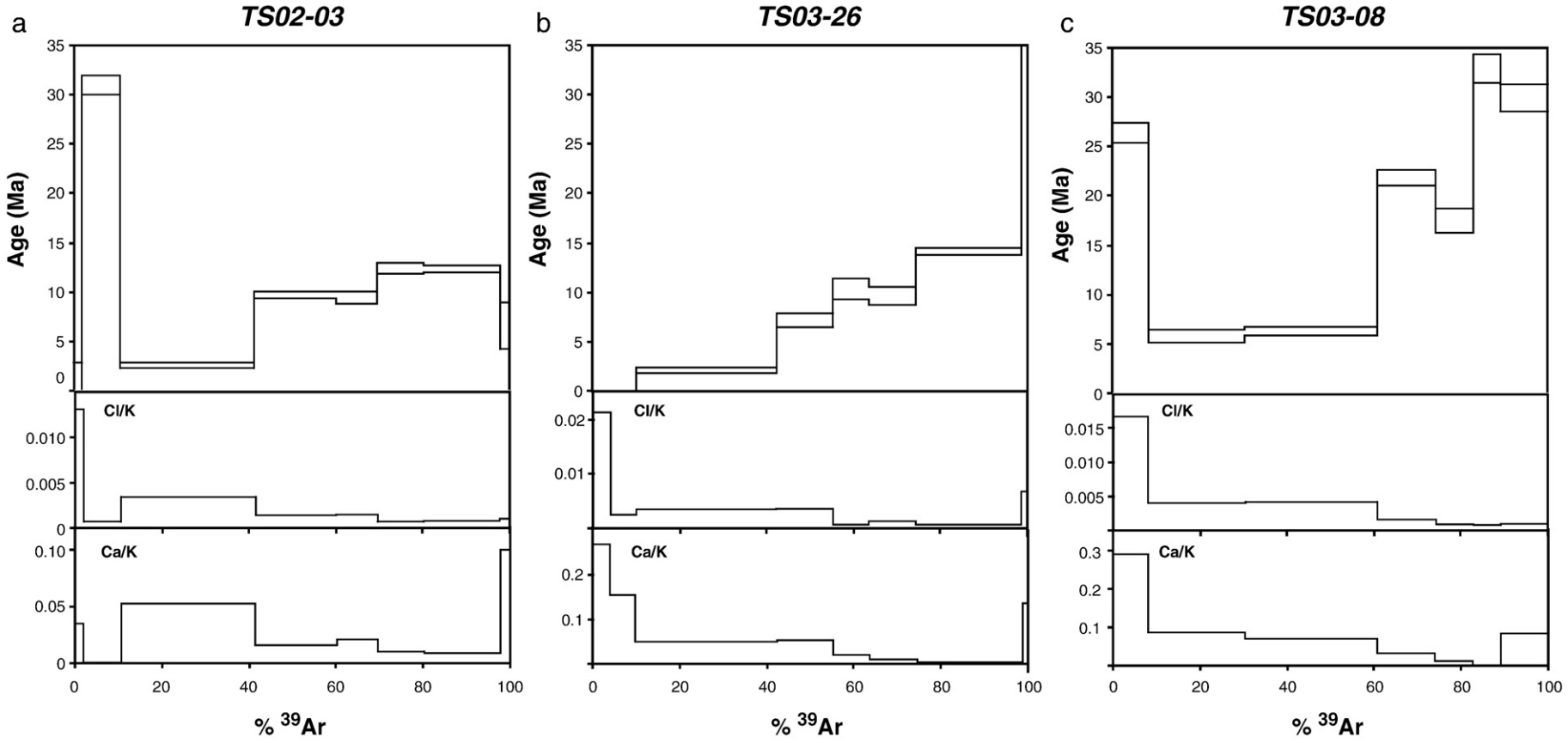

Fig. 5. $^{40}Ar/^{39}Ar$ age spectra, Cl/K and Ca/K spectra for the Ras Afraou samples. (a) Sample TS02-03, (b) Sample TS03-26, (c) Sample TS03-08.

between step ages and chemical indicators). Diagnosing the presence of heterochemical alteration phases, which are ubiquitous but minor in our samples, is possible using the Ca/K and Cl/K ratios. This also allows ruling out recoil artefacts (which aren't expected in our comparatively coarse samples).

4.2. $^{40}Ar/^{39}Ar$ results

4.2.1. Ras Afraou unit

The spectra from the 3 Ras Afraou samples (TS02-03, TS03-08, TS03-26) show a similar pattern, with hump-shaped or staircase-shaped age spectra (Fig. 5a,b,c). Both these shapes have long been demonstrated to be due to the coexistence of at least two diachronic mica generations (Wijbrans and McDougall, 1986; Villa et al., 1997). Indeed, our microstructural and microchemical observations fully confirm this. The Cl/K and Ca/K values also show a similar evolution with higher values associated with the first heating steps and decreasing toward higher degassing temperatures (Figs. 5 and 6 and Table 3).

4.2.1.1. Sample TS02-03. The good linear anticorrelation of step ages with both the Ca/K and Cl/K ratios (Fig. 6a,b) is a strong evidence that (aside from the obvious, minor alterations, diagnosed by their devious Ca/Cl ratios and ages) the Ar budget of this sample is dominated by two reservoirs. The low-Ca, low-Cl one is presumably the true muscovite. Because the correlation line is defined by a segment representing the mixture, the pure muscovite reservoir should lie to the left of the step with the lowest *x* value (Ca/K or Cl/K ratio). The exact age can only be estimated if one were to know the exact *x* value of the pure muscovite. As all we know is that the *x* value is between 0 and the value of the 950 °C step, so that the corresponding age must be between 12.4 and 15 Ma. Clays (illite, kaolinite) have low K, therefore their Ca/K and Cl/K ratios are higher (but unconstrained). Due to this lack of constraint, the age of the argillic fraction is also unconstrained; it could range between ca. 5 Ma and zero.

4.2.1.2. Sample TS03-26. The linear anticorrelation of ages with both the Ca/K and Cl/K ratios (Fig. 6c,d) is very similar to sample TS02-03, but shows the presence of a third reservoir that drags some of the points off the simple binary mixing line. This is in agreement with the petrographic observations (see above). The age of the "true muscovite" (the low-Ca, low-Cl reservoir) is identical to that of TS02-03, 12.5–15 Ma.

4.2.1.3. Sample TS03-08. The apparent ages of the high-Ca, high-Cl reservoir (identified as clayey alteration minerals) are around 6 Ma, similar to those of the two previous samples (Fig. 6e,f). However, the low-Ca, low-Cl "muscovite" ages vary erratically up to ca. 33 Ma; it is possible that these high apparent ages are either due to inheritance of older phengites or to kaolinitization (which was most extensive in this sample, see above) and attending K loss.

4.2.2. Tres Forcas unit

Samples form the Tres Forcas unit were analysed twice; the first set of analyses (TF02-02a and TF02-08a) was contemporaneous to the TS samples (Table 2), and the second set (denoted by suffix b), was preceded by supplementary hand-picking to attempt removing some of the contaminant phases. This was at least partly successful, as demonstrated by the higher K concentrations of the (b) aliquots. Furthermore this second set was analysed with more heating steps, in order to better identify several white micas generations.

4.2.2.1. Sample TF02-02. The overall shape of the duplicate analyses is well reproduced (Fig. 7a). Similarly to the TS samples, there is a negative correlation between ages and Cl/K and Ca/K ratios (Fig. 8a,b). Taking into account the petrographic observation that this sample contains one clay and three mica populations (Tables 1 and 2), namely kaolinite, muscovite, phengite relics, and paragonite, a simple binary mixing is not expected. Indeed, mixing between at least three components is visible, especially in the graph relating age to Ca/K (a stoichiometric component in paragonite). The inferred age for the low-Cl, low-Ca "muscovite" is ca. 13–14 Ma. The most Ca-rich and Cl-rich steps have ages around or below 5 Ma, similarly to the TS samples.

4.2.2.2. Sample TF02-08. Both spectra show upward convex shapes and similar ages are observed (Fig. 7b). Like TF02-02, this sample contains four phyllosilicate generations: kaolinite, muscovite, phengite relics, and paragonite. Therefore the correlation diagrams of Fig. 8c,d show no linear trend. The Ca-poor, Cl-poor "muscovite" has an ill-defined, higher apparent age than that of TF02-02. The "clayey" reservoir is as young as in the other samples.

4.2.2.3. Sample TF03-01. During the analysis of this sample, a very large fraction of the ^{39}Ar was released in one step (Fig. 7c). As this step has very low Ca/K and Cl/K ratios, we propose that its age be considered as that of the "true muscovite" as has been done for samples TS02-03 and TS03-26. This step age of 13.2 +/− 0.14 Ma (2σ uncertainty) is very similar to that of the other low-Ca, low-Cl reservoirs identified as "muscovite". The correlation between ages and Cl/K and Ca/K ratios is also similar to the TF02-02 and TF02-08 samples (Fig. 8e,f).

4.3. Relation between Ar systematics and mineral chemistry

The Ras Afraou and Tres Forcas samples show a good correlation between the Ca/K and Cl/K ratios (Fig. 9). This indicates that the most relevant process is removal of K during kaolinitization, as removal of K produces a correlated increase in both axes. The admixture of paragonite (high Ca/K) is also visible.

4.4. Summary of results

All samples show similar petrography, i.e. a mixture of at least two and at most four phyllosilicate generations. Accordingly, their Ar isotopic systematics show strong similarities. The steps with the lowest Cl/K and Ca/K ratios define ages around 12.5–15 Ma in four out of six samples (Figs. 6g,h and 8g,h). We interpret this chemical signature as that of the texturally predominant muscovite (i.e. in the foliation) and therefore the Early Miocene ages as the age of ductile deformation. Ages with low Cl/K and Ca/K ratios in the range 20–33 Ma are also observed in samples TF02-08 and TS03-08, and may represent relics of precisely that phengite generation (Figs. 6e,f and 8c,d). The steps with higher Cl/K and Ca/K ratios and ages <6 Ma probably reflect alteration of pre-existing micas by late crystallisation of illite–smectite interlayers and/or kaolinite (Figs. 6g,h and 8g,h).

5. Discussion

5.1. Geological interpretation of the $^{40}Ar/^{39}Ar$ ages

Combining the petrographic observations with the $^{40}Ar/^{39}Ar$ spectra, it is possible to propose the following interpretations:

5.1.1. Age of MP–LT metamorphism

Samples TF02-08 and TS03-08 provide constraints on the MP–LT metamorphic episode. The upward convex shape of sample TF02-08, characteristic of muscovite–phengite mixing, gives a minimum age of 23 Ma for the MP–LT event, corresponding to the Si-rich mica generation of this sample. Similar ages are obtained in sample TS03-08, with similar chemical characteristics (i.e. low Cl/K and Ca/K ratios), in the range 17.5–33 Ma. The oldest ages, around 30–33 Ma (last degassing steps) could be interpreted as relics of Si-rich micas similar to those observed in sample TF02-08. However, no clear petrographic evidence of Si-rich phengite relics has been found in this sample.

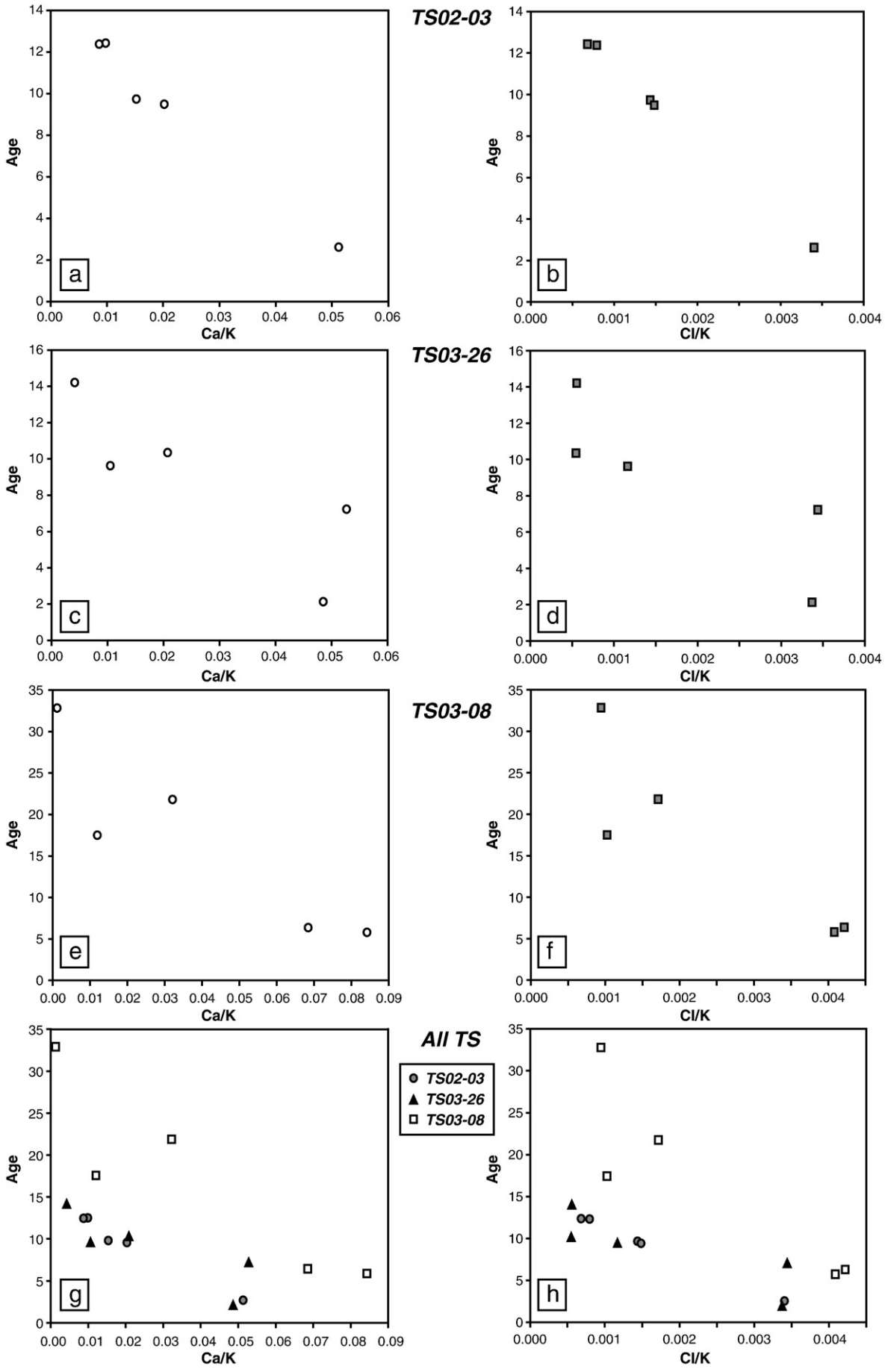
TS02-03
TS03-26
TS03-08
All TS
TS02-03
TS03-26
TS03-08
Age
Ca/K
Cl/K
a
b
c
d
e
f
g
h

Therefore we propose that the MP–LT record in the Temsamane is Oligocene in age, ca. 23 Ma old, conservatively Chattian, possibly even as old as 30 Ma.

5.1.2. Age of the ductile deformation: E–W extension and top-to-the-west senses of shear

Although Oligocene ages are observed in samples TF02-08 and TS03-08, most of the ages associated to the low-Ca, low-Cl steps in all the samples are in the range 12.5–15 Ma. These ages correspond to the low-Si mica generation in sample TF02-08 which define the base of the upward convex spectra, and appear also in all the other samples. We interpret these ages as corresponding to the muscovitic white mica generation defining the main foliation in the different samples. Therefore the main phase of E–W ductile stretching and top-to-the-west sense of shear should have taken place during the Middle Miocene (Langhian–Serravalian) and may have started somewhat earlier at the beginning of the Miocene. Consistently, apatite fission-track dating for the Ketama unit (Fig. 2) points to ages between 20 and 14 Ma (Azdimousa et al., 1998), suggesting that these units were near the surface while the MP–LT Temsamane units were being exhumed.

5.1.3. The evolution towards brittle deformation

One striking feature of the dated samples is the presence of young ages at the beginning of the $^{40}Ar/^{39}Ar$ spectra, always associated with higher Cl/K and Ca/K ratios. In sample TS03-08, theses ages (ca. 6 Ma) account for a significant part (>50%) of the released ^{39}Ar. Based on their chemical signature, we propose that these ages correspond to abundant, late argillification (illite–smectite interlayer and/or kaolinite). Our samples all have substoichiometric K concentrations, which is evidence of significant alteration. We extend this interpretation to the other samples where similar ages and chemical signatures are observed. From a tectonic point of view, the evolution towards brittle deformation with the same E–W direction of stretching (Negro et al., 2007), may have occurred between 10 and 7–6 Ma (Tortonian). This interpretation is consistent with the occurrence of unconformable Messinian sediments on top of the MP–LT Temsamane. Volcanic activity in the surrounding areas (Fig. 2), in the range 10–2.6 Ma (El Bakkali et al., 1998 and references therein) is very unlikely to have affected secondary phyllosilicate crystallisation in the dated samples.

5.2. Correlation of main tectonic and metamorphic events in the Betic–Rif arc

In order to integrate our new $^{40}Ar/^{39}Ar$ data on the Temsamane at a regional scale, we made a compilation of the available geochronological and stratigraphic constraints in the whole Betic–Rif orogen (Fig. 10). We also added the main tectonic and metamorphic event recorded in the Alboran Domain units in order to compare them with the tectono-metamorphic history of the Alboran domain (Fig. 10).

The following observations can be pointed out:

(1) The Oligocene age obtained in the Temsamane for the MP–LT metamorphism, is similar to the Eocene–Oligocene age (still debated) of the HP–LT event in the Alpujárride–Sebtide complex. Therefore a common timing for thickening episode can be proposed for the upper Alboran Domain and the Temsamane units (Fig. 10).

(2) The exhumation of the Temsamane units, dated Middle Miocene took place after the Alpujárride–Sebtide one, dated Late Oligocene–Early Miocene (Fig. 10). Furthermore the tectonic patterns accompanying exhumation show different (almost orthogonal) kinematics. However brittle deformation on low-angle normal faults in the Alpujárride in the Betics, indicate compatible ENE–WSW extension during the same period (Crespo Blanc, 1995; Martínez-Martínez and Azañon, 1997; Azañón and Crespo-Blanc, 2000) (Fig. 10).

(3) The exhumation of the Nevado–Filábride Complex (Lower Alboran Domain), characterized by ~E–W stretching and top-to-the-west senses of shear, dated Middle Miocene, is synchronous with the Temsamane and show similar kinematics (Galindo-Zaldívar et al., 1989; García-Dueñas et al., 1992; Jabaloy et al., 1993; Martínez-Martínez and Azañon, 1997; Martínez-Martínez et al., 2002; Augier et al., 2005) (Fig. 10).

5.3. Geodynamic implications on the building of the Betic–Rif arc

Our new $^{40}Ar/^{39}Ar$ data obtained in the External Rif allow to draw some regional interpretations and geodynamic implications on the building of the Betic–Rif arc. We show that ENE–WSW extension is recorded in the External Rif during the Miocene and that similar deformation is observed in the Lower Alboran Domain units in the Betics. Moreover the brittle deformation recorded in the Alpujárride Complex (Upper Alboran Domain), which has already been exhumed since the Early Miocene, shows similar direction of extension during the Serravallian–Lower Tortonian (13.7–7.2 Ma) (García-Dueñas et al., 1992; Crespo Blanc, 1995, Martínez-Martínez and Azañon, 1997) (Figs. 10 and 11). Therefore ~E–W extension is recorded simultaneously on both sides of the Gibraltar arc during the Miocene (Fig. 11). Similar ~E–W extension is also reported offshore on the Algerian margin farther east (Mauffret et al., 2004). We interpret this regional ~E–W as the result of back-arc deformation of an east dipping subduction zone rolling back towards the west during the Middle to Late Miocene as recently proposed by several authors (Lonergan and White, 1997; Martínez-Martínez and Azañon, 1997; Frizon de Lamotte et al., 2000; Duggen et al., 2004; Faccenna et al., 2004; Jolivet et al., 2006; Martínez-Martínez et al., 2006; Balanyá et al., 2007; Booth-Rea et al., 2007; Mauffret et al., 2007).

6. Conclusions

Coupling a detailed petrological study with a step heating $^{40}Ar/^{39}Ar$ dating method allowed us to date the different metamorphic events that affected the Temsamane unit even if they were partly overprinted during the retrogression.

The new $^{40}Ar/^{39}Ar$ data presented in this study provide important constraints on the timing of deformation in the External Rif and the geodynamic evolution of the Betic–Rif arc.

Three groups of $^{40}Ar/^{39}Ar$ ages can be pointed out: (1) >23 Ma corresponding to Si-rich relic micas corresponding to the highest-pressure event recorded by these units, (2) 15–12.5 Ma corresponding to the micas defining the foliation and (3) <6 Ma corresponding to late alteration phyllosilicates. Based on the $^{40}Ar/Ar\ ^{39}Ar$ ages we propose the following evolution for the Temsamane units: (1) an Oligocene

Fig. 6. Three-isotope correlation diagrams for the samples in Fig. 5. Steps clearly pertaining to alteration phases and/or plagioclase microinclusions can be diagnosed from their devious Ca/Cl ratios (Table 3); they account for a minor part of the Ar budget and are not shown. (a) Ca/K vs age correlation for sample TS02-03. The good linearity indicates that this sample consists mainly of only two generations. The age of the "true" metamorphic muscovite (the reservoir with lowest Ca/K ratios) could be determined if a precise electron microprobe determination of the Ca/K ratio in the mica were available. With the present resolution of electron microprobes, the age can be estimated to lie between ca. 12.4 Ma (if the Ca/K ratio of the muscovite is 9 E-3) and ca. 15 Ma (if the Ca/K ratio is exactly zero). (b) Cl/K vs age correlation for sample TS02-03. Similarly to Fig. 6a, the age can be estimated to lie between ca. 12.4 Ma (if the Cl/K ratio of the muscovite is 7 E-4) and ca. 15 Ma (if the Cl/K ratio is exactly zero) (c) Ca/K vs age, and (d) Cl/K vs age correlations for sample TS03-26. An extrapolation to ca. 15 Ma, similar to sample TS02-03, is compatible with the trend. (e) Ca/K vs age, and (f) Cl/K vs age correlations for sample TS03-08. All low-Ca, low-Cl points have ages between 17 and 33 Ma, with the zero-Ca extrapolation at ca. 33 Ma. (g) Ca/K vs age, and (h) Cl/K vs age correlations for all the TS samples. The TS03-08 sample shows a strikingly different pattern compared to the TS02-03 and TS03-26 samples.

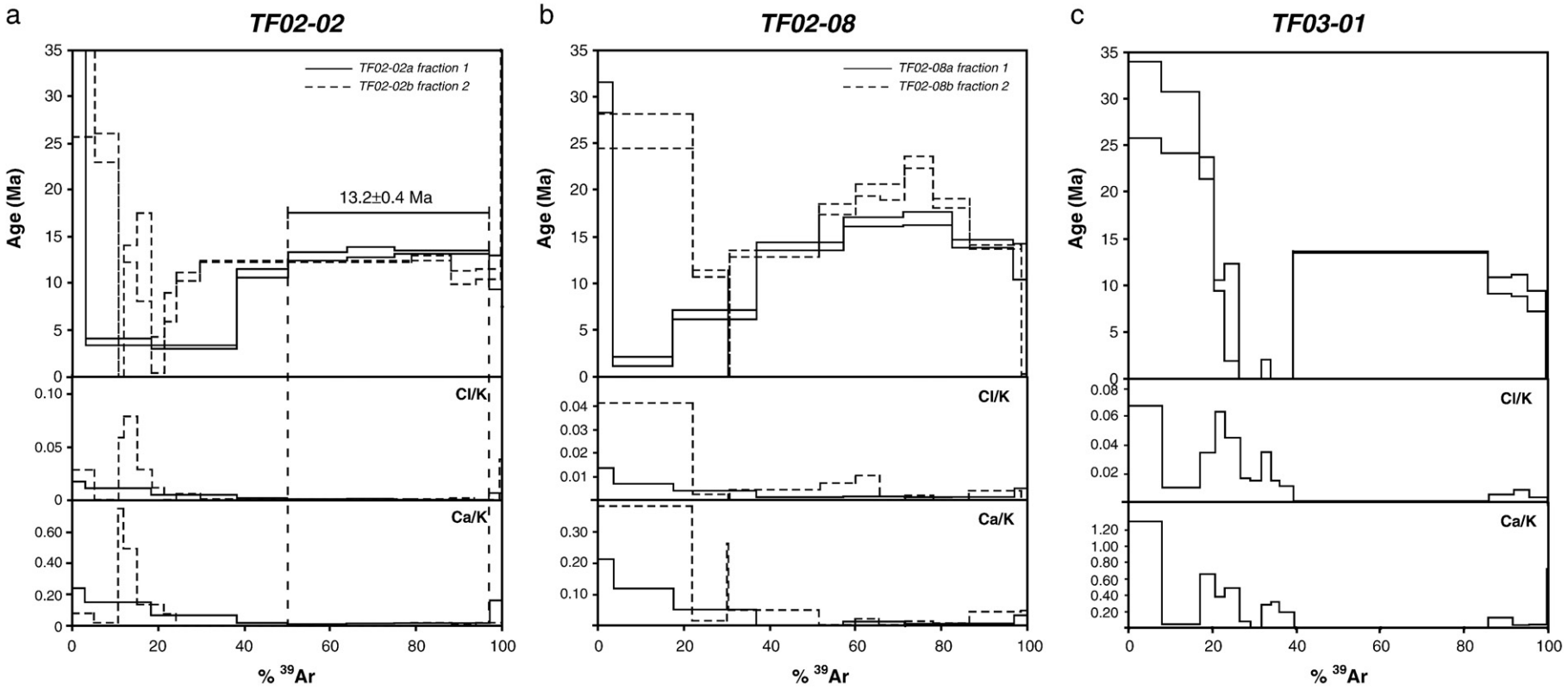

Fig. 7. $^{40}Ar/^{39}Ar$ age spectra, Cl/K and Ca/K ratios for the Tres Forcas TF02-02 (a), TF02-08 (b) and TF03-01 (c) samples.

MP–LT metamorphic event in the External Rif, highlighting a subduction event (or stacking event) during this period which could be almost contemporaneous with the burial of HP–LT units from the internal Rif (Alboran Domain), (2) a Middle to Late Miocene exhumation, characterized by an intense E–W stretching (and associated schistosity development) and by top-to-the-west shear senses, evolving towards brittle conditions.

Regional correlations show that this deformation is diachronous with the upper Alboran Domain units from the Rif and the Betics but contemporaneous and similar to the one observed in the Lower Alboran Domain units in the Betics. We show that a regional ~E–W extension is regionally recorded on both sides of the Betic–Rif arc during the Middle to late Miocene, and interpret this deformation as the result of the westward roll-back of an east dipping subduction zone during this period.

Acknowledgments

The French–Moroccan programme "Action Intégrée MA/01/13" and the CNRS-INSU are gratefully acknowledged for financial support during field and laboratory work. We warmly thank Roland Caron for the quality and the number of thin sections, and François Senebier for mineral separation. We thank F. Jourdan, I. Buick and an anonymous reviewer for their constructive comments on the manuscript.

References

Aguado, R., Feinberg, H., Durand-Delga, M., Martin-Algarra, A., Esteras, M., Didon, J., 1990. Nuevos datos sobre la edad de las formaciones miocenas transgresivas sobre las zonas internas Beticas; la Formacion de San Pedro de Alcantara (Provincia de Malaga). Revista de la Sociedad Géologica de España 3, 79–85.

Andriessen, P.A.M., Zeck, H.P., 1996. Fission-track constraints on timing of Alpine nappe emplacement and rates of cooling and exhumation, Torrox area, Betic Cordilleras, S. Spain. Chemical Geology 131, 199–206.

Andriessen, P.A.M., Hebeda, E.H., Simon, O.J., Verschure, R.H., 1991. Tourmaline K–Ar ages compared to other radiometric dating systems in alpine anatectic leucosomes and metamorphic rocks (Cyclades and southern Spain). Chemical Geology 91, 33–48.

Andrieux, J., 1973. Sur le metamorphisme des zones externes du Rif, L'Arc de Gibraltar. Bulletin de la Société Géologique de France 15, 106–107.

Augier, R., Agard, P., Monié, P., Jolivet, L., Robin, C., Booth-Rea, G., 2005. Exhumation, doming and slab retreat in the Betic Cordillera (SE Spain): in situ Ar-40/Ar-39 ages and P–T–d–t paths for the Nevado–Filabride complex. Journal of Metamorphic Geology 23, 357–381.

Azañón, J.M., Crespo-Blanc, A., 2000. Exhumation during a continental collision inferred from the tectonometamorphic evolution of the Alpujarride Complex in the central Betics (Alboran Domain, SE Spain). Tectonics 19, 549–565.

Azdimousa, A., Bourgois, J., Poupeau, G., Montigny, R., 1998. Histoire thermique du massif de Ketama (Maroc); sa place en Afrique du Nord et dans les Cordilleres betiques. Comptes Rendus de l'Academie des Sciences, Serie II 326, 847–853.

Balanyá, J.C., García-Dueñas, V., Azañón, J.M., SanchezGomez, M., 1997. Alternating contractional and extensional events in the Alpujarride Nappes of the Alboran domain (Betics, Gibraltar arc). Tectonics 16, 226–238.

Balanyá, J.C., Crespo-Blanc, A., Díaz Azpiroz, M., Expósito, I., Luján, M., 2007. Structural trend line pattern and strain partitioning around the Gibraltar Arc accretionary wedge: insights as to the mode of orogenic arc building. Tectonics 26.

Blanco, M.J., Spakman, W., 1993. The P-wave velocity structure of the mantle below the Iberian peninsula — evidence for subducted lithosphere below Southern Spain. Tectonophysics 221, 13–34.

Booth-Rea, G., Azañón, J.M., Martínez-Martínez, J.M., Vidal, O., García-Dueñas, V., 2005. Contrasting structural and *P–T* evolution of tectonic units in the southeastern Betics: key for understanding the exhumation of the Alboran Domain HP/LT crustal rocks (western Mediterranean). Tectonics 24.

Booth-Rea, G., Ranero, C.R., Martínez-Martínez, J.M., Grevemeyer, I., 2007. Crustal types and Tertiary tectonic evolution of the Alboran sea, western Mediterranean. Geochemistry Geophysics Geosystems 8, Q10005.

Calvert, A., Sandvol, E., Seber, D., Barazangi, M., Roecker, S., Mourabit, T., Vidal, F., Alguacil, G., Jabour, N., 2000. Geodynamic evolution of the lithosphere and upper mantle beneath the Alboran region of the western Mediterranean: Constraints from travel time tomography. Journal of Geophysical Research-Solid Earth 105, 10871–10898.

Chalouan, A., Michard, A., Feinberg, H., Montigny, R.A., Saddiqi, O., 2001. The Rif mountain building (Morocco): a new tectonic scenario. Bulletin de la Société Géologique de France 172, 603–616.

Crespo Blanc, A., 1995. Interference pattern of extensional fault systems: a case study of the Miocene rifting of the Alboran basement (North of Sierra Nevada, Betic Chain). Journal of Structural Geology 17, 1559–1569.

Crespo-Blanc, A., Orozco, M., García-Dueñas, V., 1994. Extension versus compression during the Miocene tectonic evolution of the Betic Chain. Late folding of normal fault systens. Tectonics 13, 78–88.

De Jong, K., 2003. Very fast exhumation of high-pressure metamorphic rocks with excess Ar-40 and inherited Sr-87, Betic Cordilleras, southern Spain. Lithos 70, 91–110.

De Jong, K., Wijbrans, J.R., Feraud, G., 1992. Repeated thermal resetting of phengites in the Mulhacen Complex (Betic Zone, southeastern Spain) shown by Ar-40/Ar-39 step heating and single grain laser probe dating. Earth and Planetary Science Letters 110, 173–191.

Duggen, S., Hoernle, K., van den Bogaard, P., C., H., 2004. Magmatic evolution of the Alboran region: The role of subduction in forming the western Mediterranean and causing the Messinian salinity crisis. Earth and Planetary Science Letters 218, 91–108.

Durand-Delga, M., Feinberg, H., Magne, J., Olivier, P., Anglada, R., 1993. Les formations oligo-miocènes discordantes sur les Malaguides et les Alpujarrides et leurs implications dans l'évolution géodynamique des Cordillères Bétiques (Espagne) et de la Mediterranée d'Alboran. Comptes Rendus de l'Académie des Sciences, Série II 317, 679–687.

El Bakkali, S., Gourgaud, A., Bourdier, J.L., Bellon, H., Gundogdu, N., 1998. Post-collision neogene volcanism of the Eastern Rif (Morocco): magmatic evolution through time. Lithos, 45, 523–543.

Esteban, J.J., Sánchez-Rodríguez, L., Seward, D., Cuevas, J., Tubía, J.M., 2004. The late thermal history of the Ronda area, southern Spain. Tectonophysics 389, 81–92.

Faccenna, C., Piromallo, C., Crespo-Blanc, A., Jolivet, L., Rossetti, F., 2004. Lateral slab deformation and the origin of the Western Mediterranean arcs. Tectonics 23. doi:10.1029/2002TC001488.

Feinberg, H., Maate, A., Bouhdadi, S., Durand-Delga, M., Maate, M., Magne, J., Olivier, P.,
1990. Signification des dépôts de l'Oligocène supérieur-Miocène inférieur du Rif interne (Maroc) dans l'évolution géodynamique de l'arc de Gibraltar. Comptes Rendus de l'Académie des Sciences, Série II 310, 1487–1495.

Frizon de Lamotte, D., 1985. La structure du Rif Oriental (Maroc): rôle de la tectonique longitudinale et importance des fluides. PhD thesis, Université Pierre et Marie Curie, Paris, 436 pp.

Frizon de Lamotte, D., 1987. La structure du Rif externe (Maroc); mise au point sur le role des decrochements des chevauchements et des glissements gravitaires (Structure of the Rif external zones; evidence on the role of overthrusting and gravity sliding). Journal of African Earth Sciences 6, 755–766.

Frizon de Lamotte, D., Saint Bezar, B., Bracene, R., Mercier, E., 2000. The two main steps of the Atlas building and geodynamics of the western Mediterranean. Tectonics 19, 740–761.

Frizon de Lamotte, D., Crespo-Blanc, A., Saint-Bézar, B., Comas, M., Fernàndez, M., Zeyen, H., Ayarza, P., Robert-Charrue, C., Chalouan, A., Zizi, M., Teixell, A., Arboleya, M.L., Alvarez-Lobato, F., Julivert, M., Michard, A., 2004. Transect I: Iberia–Meseta–Guadalquivir Basin–Betic Cordillera–Alboran Sea–Rif–Moroccan Meseta–High Atlas–Sahara Domain. In: Cavazza, W., Roure, F.M., Spakman, W., Stampfli, G.M., Ziegler, P.A. (Eds.), The TRANSMED Atlas — The Mediterranean Region from Crust to Mantle. Springer, Berlin, Heidelberg.

Galindo-Zaldívar, J., Gonzalez-Lodeiro, F., Jabaloy, A., 1989. Progressive extensional shear structures in a detachment contact in the Western Sierra Nevada (Betic Cordilleras, Spain). Geodinamica Acta 3, 73–85.

García-Dueñas, V., Balanyá, J.C., Martínez-Martínez, J.M., 1992. Miocene extensional detachments in the outcropping basement of the Northern Alboran Basin (Betics) and their tectonic implications. Geo Marine Letters 12, 88–95.

Goffé, B., Michard, A., García-Dueñas, V., Gonzalez-Lodeiro, F., Monié, P., Campos, J., Galindo-Zaldívar, J., Jabaloy, A., Martínez-Martínez, J.M., Simancas, J.F., 1989. First evidence of high-pressure, low-temperature metamorphism in the Alpujarride nappes, Betic Cordilleras (S. E. Spain). European Journal of Mineralogy 1, 139–142.

Gómez-Pugnaire, M.T., Fernandez Soler, J.M., 1987. High-pressure metamorphism in metabasites from the Betic Cordilleras (SE Spain) and its evolution during the alpine orogeny. Contributions to Mineralogy and Petrology 95, 231–244.

Jabaloy, A., Galindo-Zaldívar, J., Gonzalez-Loreiro, F., 1993. The Alpujarride–Nevado–Filabride extensional shear zone, Betic Cordillera, SE Spain. Journal of Structural Geology 15, 555–569.

Janots, E., Negro, F., Brunet, F., Goffe, B., Engi, M., Bouybaouene, M.L., 2006. Evolution of the REE mineralogy in HP–LT metapelites of the Sebtide complex, Rif, Morocco: monazite stability and geochronology. Lithos 87, 214–234.

Johnson, C., Harbury, N., Hurford, A.J., 1997. The role of extension in the miocene denudation of the Nevado–Filabride complex, Betic Cordillera (SE Spain). Tectonics 16, 189–204.

Jolivet, L., Augier, R., Robin, C., Suc, J.P., Rouchy, J.M., 2006. Lithospheric-scale geodynamic context of the Messinian salinity crisis. Sedimentary Geology 188–189, 9–33.

Kelley, S., Turner, G., Butterfield, A.W., Shepherd, T.J., 1986. The source and significance of argon isotopes in fluid Inclusions from areas of mineralization. Earth and Planetary Science Letters 79, 303–318.

Lonergan, L., White, N., 1997. Origin of the Betic–Rif mountain belt. Tectonics 16, 504–522.

Martínez-Martínez, J.M., Azañon, J.M., 1997. Mode of extensional tectonics in the southeastern Betics (SE Spain): implications for the tectonic evolution of the peri-Alboran orogenic system. Tectonics 16, 205–225.

Martínez-Martínez, J.M., Soto, J.I., Balanyá, J.C., 2002. Orthogonal folding of extensional detachments: structure and origin of the Sierra Nevada elongated dome (Betics, SE Spain). Tectonics 21.

Martínez-Martínez, J.M., Booth-Rea, G., Azañón, J.M., Torcal, F., 2006. Active transfer fault zone linking a segmented extensional system (Betics, southern Spain): insight into heterogeneous extension driven by edge delamination. Tectonophysics 422, 159–173.

Mauffret, A., de Lamotte, D.F., Lallemant, S., Gorini, C., Maillard, A., 2004. E–W opening of the Algerian Basin (Western Mediterranean). Terra Nova 16, 257–264.

Mauffret, A., Ammar, A., Gorini, C., Jabour, H., 2007. The Alboran Sea (Western Mediterranean) revisited with a view from the Moroccan Margin. Terra Nova 19, 195–203.

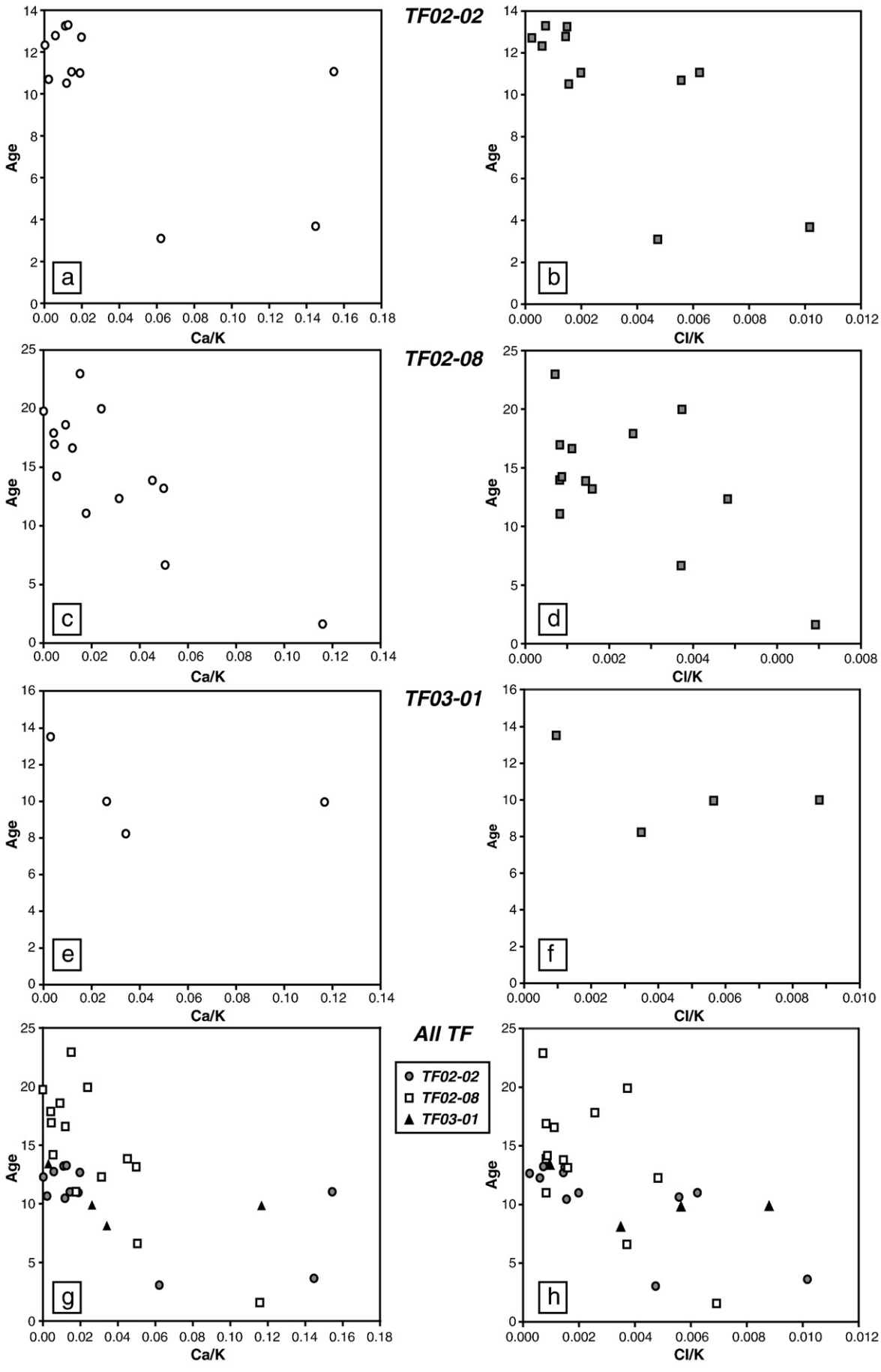
TF02-02
TF02-08
TF03-01
All TF
TF02-02
TF02-08
TF03-01
Age
Ca/K
Cl/K
a
b
c
d
e
f
g
h

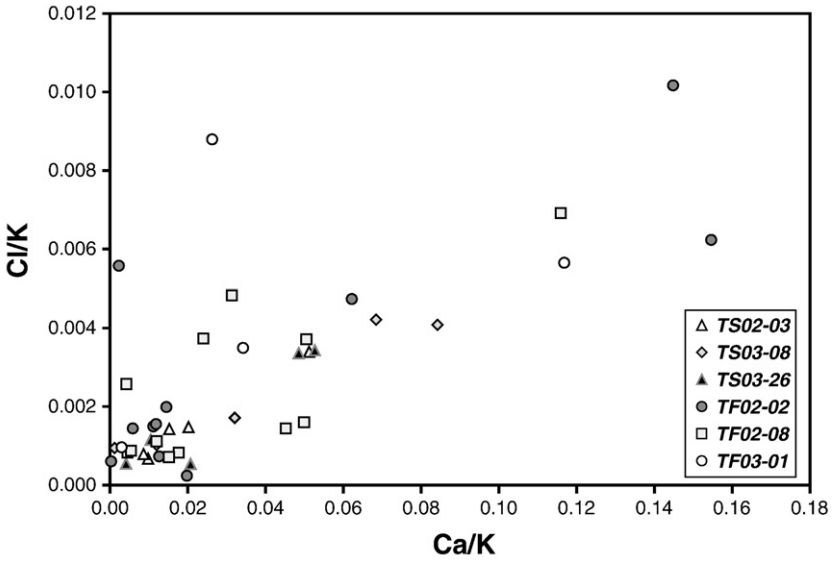

Fig. 9. Ca/K vs Cl/K correlation diagram for all the samples. The teoretical stoichiometry of ideal muscovite would plot exactly at the origin. Contaminant phases are seen to be heterogeneous, as shown by the fanning out of some (low-temperature) steps; the major part of the Ar release plots along sample-specific linear correlation trends. This indicates that each sample is principally composed of a binary mixture.

Mayoral, E., Crespo-Blanc, A., Gracia Diaz, M., Benot, C., Orozco, M., 1994. Rifting miocène du Domaine d'Alboran: Datations de sédiments discordants sur les unités Alpujarrides en extension (Sud de la Sierra Nevada, Chaine Bétique). Compte Rendus de l'Académie des Sciences, Série II 319, 581–588.

Merrihue, C., Turner, G., 1966. Potassium–argon dating by activation with fast neutrons. Journal of Geophysical Research 71, 2852–2857.

Michard, A., Negro, F., Saddiqi, O., Bouybaouène, M.L., Chalouan, A., Montigny, R., Goffé, B., 2006. Pressure–temperature-time constraints on the Maghrebide mountain building: evidence from the Rif–Betic transect (Morocco, Spain), Algerian correlations, and geodynamic implications. Comptes Rendus Géoscience 338, 92–114.

Monié, P., Frizon de Lamotte, D., Leikine, M., 1984. Etude géochronologique préliminaire par la méthode 39Ar/40Ar du métamorphisme alpin dans le rif externe (Maroc); précisions sur le calendrier tectonique tertiaire. Revue de Géologie Dynamique et de Géographie Physique 25, 307–317.

Monié, P., Galindo-Zaldívar, J., Lodeiro, F.G., Goffé, B., Jabaloy, A., 1991. Ar-40/Ar-39 geochronology of Alpine tectonism in the Betic Cordilleras (Southern Spain). Journal of the Geological Society 148, 289–297.

Monié, P., Torres-Roldán, R.L., García-Casco, A., 1994. Cooling and exhumation of the Wertern Betic Cordilleras, 40Ar/39Ar thermochronological constraints on a collapsed terrane. Tectonophysics 238, 353–379.

Montenat, C., Ott d'Estevou, P., 1999. The diversity of late neogene sedimentary basins generated by wrench faulting in the eastern Betic Cordillera, SE Spain. Journal of Petroleum Geology 22, 61–80.

Müller, W., Kelley, S.P., Villa, I.M., 2002. Dating fault-generated pseudotachylytes: comparison of Ar-40/Ar-39 stepwise-heating, laser-ablation and Rb–Sr microsampling analyses. Contributions to Mineralogy and Petrology 144, 57–77.

Negro, F., Beyssac, O., Goffé, B., Saddiqi, O., Bouybaouène, M.L., 2006. Thermal structure of the Alboran Domain in the Rif (northern Morocco) and the Western Betics (southern Spain). Constraints from Raman spectroscopy of carbonaceous material. Journal Of Metamorphic Geology 24, 309–327.

Negro, F., Agard, P., Goffé, B., Saddiqi, O., 2007. Tectonic and metamorphic evolution of the Temsamane units, External Rif (northern Morocco): implications for the evolution of the Rif and the Betic–Rif arc. Journal of the Geological Society 164, 829–842.

Platt, J.P., Vissers, R.L.M., 1989. Extensional collapse of thickened continental lithosphere: a working hypothesis for the Alboran Sea and Gibraltar Arc. Geology 17, 540–543.

Platt, J.P., Whitehouse, M.J., 1999. Early Miocene high-temperature metamorphism and rapid exhumation in the Betic Cordillera (Spain); evidence from U–Pb zircon ages. Earth and Planetary Science Letters 171, 591–605.

Platt, J.P., Whitehouse, M.J., Kelley, S.P., Carter, A., Hollick, L., 2003a. Simultaneous extensional exhumation across the Alboran Basin: implications for the causes of late orogenic extension. Geology 31, 251–254.

Platt, J.P., Argles, T.W., Carter, A., Kelley, S.P., Whitehouse, M.J., Lonergan, L., 2003b. Exhumation of the Ronda peridotite and its crustal envelope: constraints from thermal modelling of a *P–T*-time array. Journal of the Geological Society 160, 655–676.

Platt, J.P., Kelley, S.P., Carter, A., Orozco, M., 2005. Timing of tectonic events in the Alpujárride Complex, Betic Cordillera, S. Spain. Journal of the Geological Society, London 162, 451–462.

Platt, J.P., R., A., Soto, J.I., Kelley, S., 2006. Early Miocene continental subduction and rapid exhumation in the western Mediterranean. Geology 34, 981–984.

Poisson, A.M., Morel, J.L., Andrieux, J., Coulon, M., Wernli, R., Guernet, C., 1999. The origin and development of neogene basins in the SE Betic Cordillera (SE Spain): a case study of the Tabernas-Sorbas and Huercal Overa basins. Journal of Petroleum Geology, 22, 97–114.

Rodríguez-Fernández, J., Martín-Penela, A.J., 1993. Neogene evolution of the Campo de Dalías and the surrounding off-shore areas (Northeastern Alboran Sea). Geodinamica Acta, 6, 255–270.

Sánchez-Rodríguez, L., 1998. Pre-Alpine and Alpine evolution of the Ronda Ultramafic Complex and its country-rocks (Betic chain, southern Spain): U–Pb SHRIMP zircon and fission-track dating. PhD Thesis, Swiss Federal Institute of Technology, Zurich, 170 pp.

Seber, D., Barazangi, M., Ibenbrahim, A., Demnati, A., 1996. Geophysical evidence for lithospheric delamination beneath the Alboran Sea and Rif–Betic mountains. Nature, 379, 785–790.

Sosson, M., Morillon, A.C., Bourgois, J., Feraud, G., Poupeau, G., Saint-Marc, P., 1998. Late exhumation stages of the Alpujarride Complex (western Betic Cordilleras, Spain): new thermochronological and structural data on Los Reales and Ojen nappes. Tectonophysics, 285, 253–273.

Suter, G., 1980. Carte Géologique de la Chaîne Rifaine. Scale: 1/500 000. Editions du Service Géologique du Maroc, Notes et Mémoires, 245 a

Tubía, J.M., Cuevas, J., Esteban, J.J., 2004. Tectonic evidence in the Ronda peridotites, Spain, for mantle diapirism related to delamination. Geology 32, 941–944.

Villa, I.M., 2001. Radiogenic isotopes in fluid inclusions. Lithos 55, 115–124.

Villa, I.M., Ruggieri, G., Puxeddu, M., 1997. Petrological and geochronological discrimination of two white-mica generations in a granite cored from the Larderello–Travale geothermal field (Italy). European Journal Of Mineralogy 9, 563–568.

Villa, I.M., Hermann, J., Muntener, O., Trommsdorff, V., 2000. Ar-39–Ar-40 dating of multiply zoned amphibole generations (Malenco, Italian Alps). Contributions to Mineralogy and Petrology 140, 363–381.

Völk, H.R., 1967. Relations between Neogene sedimentation and late orogenic movements in the Eastern Betic Cordilleras (SE Spain). Geologie en Mijnbouw 46, 471–474.

Wijbrans, J.R., McDougall, I., 1986. Ar-40/Ar-39 dating of white micas from an Alpine high-pressure metamorphic belt on Naxos (Greece) — the resetting of the argon isotopic system. Contributions to Mineralogy and Petrology 93, 187–194.

Zeck, H.P., 1996. Betic–Rif Orogeny; subduction of Mesozoic Tethys lithosphere under eastward drifting Iberia, slab detachment shortly before 22 Ma, and subsequent uplift and extensional tectonics. Tectonophysics 254, 1–16.

Zeck, H.P., Albat, F., Hansen, B.T., Torres-Roldán, R.L., García-Casco, A., Martin-Algarra, A., 1989. A 21 ± 2 Ma age for the termination of the ductile Alpine deformation in the internal zone of the Betic Cordilleras, South Spain. Tectonophysics 169, 215–220.

Zeck, H.P., Monié, P., Villa, I.M., Hansen, B.T., 1992. Very high rates of cooling and uplift in the Alpine Belt of the Betic Cordilleras, Southern Spain. Geology 20, 79–82.

Fig. 8. Three-isotope correlation diagrams for samples in Fig. 7. Steps clearly pertaining to alteration phases and/or plagioclase microinclusions are not shown. (a) Ca/K vs age correlation for samples TF02-02a and 02b. The absence of a simple linearity is coherent with the observation that this sample contains at least four mica/clay generations (muscovite, phengite relics, paragonite, and kaolinite). A trend towards a low-Ca Ar reservoir aged ca.12–15 Ma is visible (cf. Fig. 6a). (b) Cl/K vs age correlation for samples TF02-02a and 02b. (c) Ca/K vs age, and (d) Cl/K vs age correlation for samples TF02-08a and 08b. (e) Ca/K vs age and (f) Cl/K vs age correlation for samples TF03-01. (g) Ca/K vs age, and (h) Cl/K vs age correlations for all TF samples. Samples TF02-02 and TF03-01 plot along the same correlation trend, while TF02-08 reflects a different inventory of Ar reservoirs. In general, the diagram shows several white micas generations with two low-Ca low-Cl reservoirs: one with a ca. 12–15 Ma age similar to the TS02-03 and TS03-26 samples and another one older than 20 Ma.

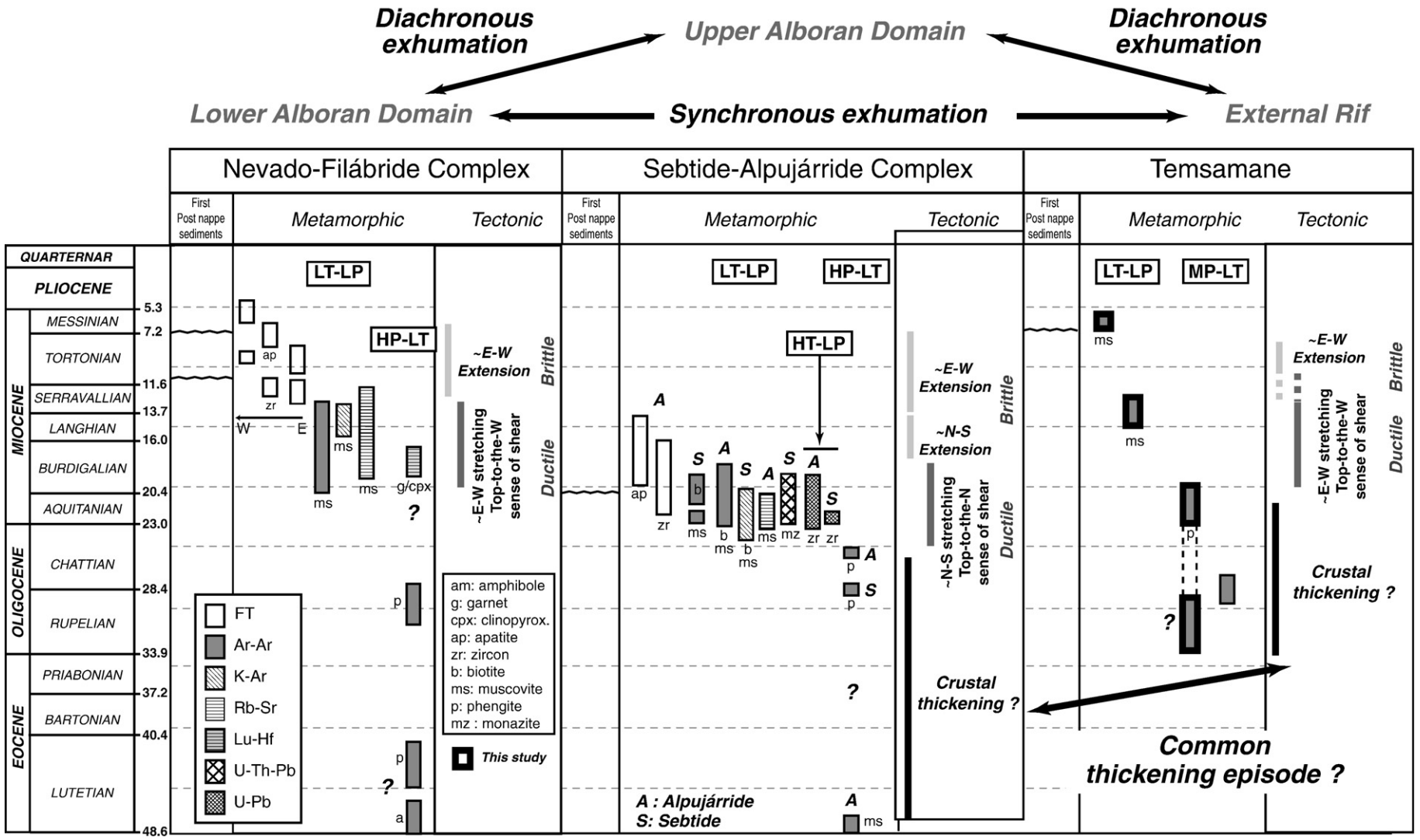

Fig. 10. Timing of tectonic and metamorphic events in the Temsamane and the Alboran Domain units (Nevado–Filábride and Alpujárride–Sebtide complexes) (see text for further details). Geochronological and stratigraphic constraints are after: *Stratigraphic*: (Völk, 1967; Aguado et al., 1990; Feinberg et al., 1990; Rodríguez-Fernández and Martín-Penela, 1993; Durand-Delga et al., 1993; Mayoralet al., 1994; Crespo-Blanc et al., 1994; Montenat and Ott d'Estevou, 1999; Poisson et al., 1999). *Fission tracks*: (Andriessen and Zeck, 1996; Johnson et al., 1997; Sosson et al., 1998; Esteban et al., 2004; Platt et al., 2003a,b, 2005). *Ar–Ar,K–Ar and Rb–Sr dating*: (Michard et al., 2006, Zeck et al., 1989, 1992; Andriessen et al., 1991;De Jong, 2003; De Jong et al., 1992; Monié et al., 1984, 1991,1994; Augier et al., 2005. Platt et al., 2003a,b, 2005). *Lu–Hf dating*: (Platt et al., 2006). *U–Pb dating*: (Sánchez-Rodríguez, 1998; Platt and Whitehouse, 1999; Platt et al., 2003a. *U–Th–Pb dating*: Janots et al., 2006). Tectonic constraints on the evolution of different units after: (Galindo-Zaldívar et al., 1989; García-Dueñas et al., 1992; Jabaloy et al., 1993; Crespo Blanc, 1995; Martínez-Martínez and Azañon, 1997; Azañón and Crespo-Blanc, 2000; Martínez-Martínez et al., 2002; Booth-Rea et al., 2005).

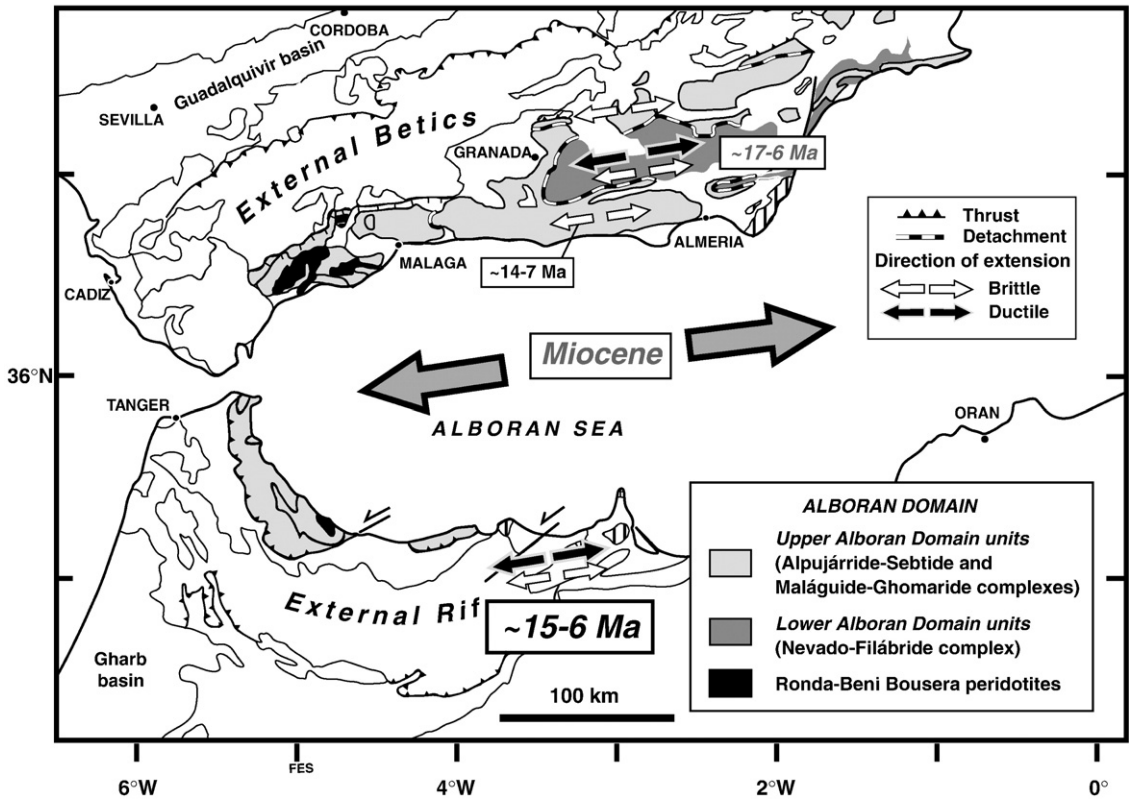

Fig. 11. Simplified tectonic map of the Betic–Rif arc. Geochronological constraints for the exhumation of the Temsamane and Nevado–Filábride Complex are reported as well as direction of ductile and brittle extension during the Miocene (see Fig. 10 for references).